The Dissertation Committee for Evangelos Anastasios Meintanis
certifies that this is the approved version of the following dissertation:

Molecular Dynamics Simulations of Metallic Friction and of its Dependence on Electric Currents - Development and First Results

Committee:

Michael Marder, Supervisor

Roger D Bengtson

John T Markert

Gregory J Rodin

Sikhanda S Satapathy

Jack B Swift

Molecular Dynamics Simulations of Metallic Friction and of its Dependence on Electric Currents - Development and First Results

by

Evangelos Anastasios Meintanis, Ptychion, MA

Dissertation

Presented to the Faculty of the Graduate School of
The University of Texas at Austin
in Partial Fulfillment
of the Requirements
for the Degree of

Doctor of Philosophy

The University of Texas at Austin

May 2009

To my parents,

The titans who kept raising the ceiling higher

Acknowledgments

I would like to thank my adviser, Prof. Michael Marder. In the best of the Socratic traditions, he provided the inspiration, intellectual stimulation, support and sound advice, to lead me into and keep me going through this beautiful garden of discovery.

This path would have been much more difficult, without the financial support secured by Dr. Sikhanda Satapathy of the Institute for Advanced Technology.

I am extremely fortunate, to have studied at the Center for Nonlinear Dynamics. Prof. Harry Swinney has permeated this great environment with the warmth and purpose of his presence. Olga Vera has been a precious source of care and support.

The example, the stamina and the hope that fueled my quest so far stem from my family and especially my parents, to whom I am deeply indebted for all that's good in me. A wonderful new presence marked the last few years of my life. Thank you Diana.

Evangelos Anastasios Meintanis

The University of Texas at Austin
May 2009

Molecular Dynamics Simulations of Metallic Friction and of its Dependence on Electric Currents - Development and First Results

Publication No. ____________________

Evangelos Anastasios Meintanis, Ph.D.
The University of Texas at Austin, 2009

Supervisor: Michael Marder

We have extended the HOLA molecular dynamics (MD) code to run slider-on-block friction experiments for Al and Cu. Both objects are allowed to evolve freely and show marked deformation despite the hardness difference. We recover realistic coefficients of friction and verify the importance of cold-welding and plastic deformations in dry sliding friction. Our first data also show a mechanism for decoupling between load and friction at high velocities. Such a mechanism can explain an increase in the coefficient of friction of metals with velocity. The study of the effects of currents on our system required the development of a suitable electrodynamic (ED) solver, as the disparity of MD and ED time scales threatened the efficiency of our code. Our first simulations combining ED and MD are presented.

Contents

Chapter 1

Introduction

1.1 Motivation

Friction is the phenomenon where two surfaces in contact resist lateral motion. The ubiquity of this effect is such that it is easy to overlook in everyday life. Still, life as we know it would be impossible without friction. Static friction in particular, the kind that creates seizure between two surfaces, enables almost all mechanical manipulations of our environment. It allows us to commute on land, whether on foot or in the majority of our vehicles. It is so hardwired into our brain that we can relate to the misadventures of slapstick comedy heroes, when its comfortable rug is pulled from under their feet and they try haphazardly to reclaim their grasp on their surroundings. When lateral motion between two surfaces has been established we speak of dynamic friction. Because this is a force exerted between objects in motion, it robs energy from our bodies and our machines while converting it to heat. More than that, it causes wear and tear that adds to other modes of material disintegration. Human ingenuity, found ways to put even that kind of friction to work. Frictional heating has been used to start fire and the application of frictional brakes allows us to control the speed of most wheeled vehicles.

The inescapable presence of friction and the multitude of uses and problems it presents, mean that man needs to be able to control it. We need to be able to reduce it when its effects are purely detrimental and to modulate it, to the levels needed, when it facilitates a particular application. Control over a phenomenon can only be the result of understanding. The multi-disciplinary research that drives the field of tribology today can only be a testament to the richness of the subject and the open frontiers that it still presents for exploration.

As with most current research, this study derives its funding from the requirements of a very specific application. The application in question is a form of electromagnetic launcher, the railgun. This launcher is being developed for the US Navy[21] by a constellation of labs around the US, one of which is the Institute for Advanced Technology at The University of Texas at Austin. The principle of operation for this launcher is illustrated in the conceptual drawing of Figure 1.1. The device consists of two parallel conducting rails that are connected to a high current power supply, e.g. a capacitor bank. The rails are electrically shorted by a slider, the armature. When current flows through the system, the counter propagating currents in the two rails produce a strong magnetic field in the space between them. It is this field that interacts with the current carrying armature and generates the Lorentz force that propels it along the rails. In an actual system, the armature is either integral to the projectile or just pushing it along the barrel of the gun.

The main advantages of the railgun over conventional guns are in safety, volume savings and higher muzzle velocity. Safety is enhanced because no chemical explosives are used as propellants. Volume savings are achieved because only shells need to be stored for a cannon to operate. Although space savings are partially

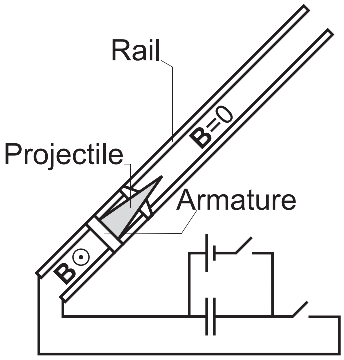

Figure 1.1: Conceptual drawing of a railgun

offset by the power supply requirements, the new generation electric ships, that are being considered by the US Navy, will already have ample resources from their nuclear reactors, to charge the necessary high current power supplies. In terms of the muzzle velocity, where conventional guns are bound by the thermodynamics of the expanding propellant gases to velocities of the order of 1km/s, electromagnetic launchers have no such theoretical limits, and muzzle velocities in excess of 2km/s have been achieved in well instrumented experiments[23]. Higher muzzle velocities translate to a combination of shorter flight time, increased range, and improved effectiveness of the projectile. The latter is due to the linearly increased momentum and quadratically increased kinetic energy imparted to it by the gun.

One of the most significant obstacles in the operational deployment of railguns is the fast rate of wear that afflicts their rails. Currently, these components need to be replaced or resurfaced every few shots. In naval applications, where railguns are proposed as replacements for large bore guns, the frequent replacement, or dismantling, of large gun barrels would be required. Such an operational handicap is unacceptable, when readiness and rate of fire are vital to the survival of the ship and the execution of its mission.

Compared to conventional gun barrels then, where lifetimes are in the order of tens of thousands of rounds for small calibers (20,000+ rounds advertised for Heckler and Koch's MP5 sub-machine gun), railguns seem to be at a distinct disadvantage. But then, it is a more complicated function that the latter are called to perform. The currents that need to flow through the rail and its contact with the armature are extremely high. In the IAT railgun, currents of the order of MA are employed, to propel an armature of approximately 200g through a barrel with a 40mm×40mm square bore. To avoid heat losses, as well as the complete meltdown of the rails, materials with high electrical and thermal conductivities need to be employed in their construction. Meanwhile, maintaining good contact between rail and armature, to facilitate the flow of the resultant current densities of order $10^8 \mathrm{A/m^2}$, requires the application of enough pressure, that, in the initial positioning of the armature within the barrel, a hydraulic ram is utilized. Even so, by the end of the armature travel, enough material has been worn out or melted that arcing is evident on the rails[7].

In trying to improve the lifetime of the rails in such a launcher, one needs to deal with a complex and multi-scale problem. Electrical current and its effects need to be considered and inform the mechanical aspects of the relevant study. In terms of scale, macroscopically, the shape and size of the armature affect the performance of the system, while the changing contact conditions along the length of the gun barrel require a balancing act in terms of both the optimal geometry as well as the optimal current delivery profile, to reduce and even out the wear. These macroscopic decisions need to be based on an understanding of the microscopic behavior of the contact between the two conductors. This is where this work attempts to provide a robust research tool and to shine some light on the atomic scale physics of friction.

For instance, our current results show that contact points which don't bear significant part of the load can develop between metallic surfaces at high velocities. Since the extent of these contacts is not dictated by the normal force, they contribute to an increase of the coefficient of friction with velocity and surface area. Characterizing such contacts would allow engineers to better quantify a balance, between the lower electrical resistance of a larger armature contact patch and its mechanical disadvantages, given that the application target velocities are considerably higher than those where we have observed the phenomenon.

Because it addresses fundamental, rather than application specific questions then, this research is valuable to the greater society. While the operating conditions in a railgun are comparatively extreme, sliding electrical contacts are rather widespread in current technological applications. Brushed DC motors and sliding electric pickups on trains and trolley cars are prime examples of devices utilizing such contacts. As with railguns, the understanding of the electromechanical tradeoffs involved can lead to better design of this equipment, to achieve target goals for efficiency or reliability.

To a research group with expertise in molecular dynamics and fracture, atomic scale friction is but a natural extension of its research. Indeed, one can view friction as the result of bond creation and breaking along the contact surfaces between objects. Adding the conductive properties of the materials in question into the mix only adds to the challenge that the problem presents.

From a personal standpoint, and beyond the trivial advantage of a research project that does receive funding, the challenge of the balancing act between theoretical accuracy and computational limitations felt and still does feel exhilarating. The inherent quest in any numerical dynamics study, such as this, is to find out how many physical laws need to enter, as well as the most efficient way to translate them into computer instructions, to simulate complex phenomena and extract useful information about them. In this way, numerical simulations also bridge the gap between theory and experiment, by providing an ideal proving ground for theories, that can be applied in a controlled environment, compared to each other and matched to observations. As the research progressed, my excitement grew stronger at what appears to be a budding field of research in dynamic friction, a phenomenon that is harder to observe microscopically than its static counterpart and ideally suited to numerical study.

1.2 A Little (Far from Exhaustive) History

To put the research described in this work in perspective and to justify its significance, a historical context is necessary. There are obviously more detailed accounts of the development of tribology and indeed the book by Dowson[10] has been the main source for the following review. While lubrication and rolling friction are also tribological subjects, this study focuses on dry sliding friction and that will be our focus here.

Evidence of the use of friction for fire starting and the production of stone tools and weapons goes back to the end of the lower paleolithic period ($\sim 2 \cdot 10^5$ years BP). Through the transition of the primitive hunter-gatherer nomad to the settler of the Mesolithic times to the more sophisticated man of Neolithic times, friction was a fact of life. While skill on the processes that utilized it seemed to improve, there are no records of attempt to control it. As food sources became more dependable though and crafts and trade started evolving in Neolithic times, we see evidence of a more conscious approach to friction. Metal linings in the sockets of pivot hinges most probably had the dual role of reducing friction and wear in the operation of the doors they supported. Spindles were required for the drills that the new crafts employed and the choice of material was very important for both the efficiency and the reliability of these tools.

The beginning of the early civilizations in Mesopotamia and Egypt, as well as in China, around the third millennium BC, solidified the conscious, if practical, approach to friction and wear. Increasingly complex machines, such as the bow drill, the potter's wheel and the wheeled vehicle required durable bearings and lubrication, the latter based mainly on water, animal fats and bitumen. The erection of the timeless monuments from that era also required more than a large supply of man power and determination. The weakness of wheeled vehicles and their unsuitability for some of the terrains through which the massive stones had to be transported meant that sliding was necessary and technical solutions were developed to facilitate the effort. Stones were placed on sledges, while planks laid on the ground, water lubrication and rolling pins were some of the means by which their motion was facilitated, according to paintings and reliefs chronicling the projects. Stone laying also utilized fluid film lubrication through the use of mortar, which allowed placement corrections before drying. The common thread in all these advances, and those that followed until the renaissance, was the lack of any fundamental understanding of friction. Humans were solving technological challenges based on experience, observation, trial and error. The adequacy of the offered solutions made fundamental questions on friction (and much of the human experience of nature for that matter) less urgent. One of the few exceptions was perhaps Aristotle's philosophical excursion into the nature of motion. Unfortunately, by his proposal that the natural kinetic state for any material object is immobility, Aristotle made friction a property of motion and muddled its identity. It is ironic, and quite unlike the man and the dialectical process from which he originated, that his effort towards the scientific understanding of nature would be used to suppress science, when his cosmology was adopted as dogma by the christian church in the middle ages. The latter period was also a time of technological backtracking in tribology. Achievements of the Greco-Roman period, such as the extensive use of metals and the employment of rolling elements in some of the most demanding bearings, all but disappeared from manufacturing practice, at least in most of Europe. There were several reasons for this. The extensive abolishment of slavery, due to the christianization of Europe, brought the loss of a major source of cheap labor and power. The unrest due to the tribal migrations from the east and the resulting increase of the population density, made sustenance more difficult and stretched the resources of raw materials. The confluence of these factors focused most economies on agriculture and most states on war preparations and away from ambitious engineering projects.

At the dawn of the Renaissance (mid 15th century AD), the new sources of raw material, that were made available by exploratory expeditions, and the widespread adoption of wind- and water-mills, which decreased the cost and increased the efficiency of both food and material processing, brought new wealth and re-established the ailing middle class in Europe. Along with it, the arts and crafts started flourishing again, and so did natural philosophy and science. Leonardo da Vinci was one of the prominent personalities of that time, recognized by his contemporaries both as an artist and an engineer. A polymath, he gave precedence to science rather than application and emphasized the value of experiment and theory. It is only in retrospect though that the full magnitude of his genius can be recognized. Much of the work included in his still surfacing codices was never published and was clearly ahead of its time. From a tribological perspective, his notes indicate that he had discovered the two laws of friction (independence from surface area and proportionality to the load) through experiments, preceding the work of G. Amontons by two centuries. His work on bearing wear, design and materials was also ahead of its time. His caged roller and split-bush bearing designs, as well as the prescription of his "mirror metal", a bronze alloy suitable for bearing construction, were to be re-invented decades or centuries later and are but some of his greatest achievements in the field. If Leonardo da Vinci's contributions lacked the reach and impact that publication would have afforded them, that wasn't the case for the work of other prominent scientists of the period. Astronomical observations and calculations by Nicolaus Copernicus, Johannes Kepler and Galileo Galilei started exposing the errors of the geocentric dogma and ushered in the era of the Scientific Revolution. Within this spirit, the error of Aristotelian mechanics with respect to the natural kinetic state of an object was to be exposed by Galileo. He demonstrated experimentally that friction and aerodynamic drag can be modulated and do not depend on intrinsic object properties. Thus, he proved that friction is a force, acting on the same footing as any other force on the motion of objects. In this way, he was the first to rigorously treat inertia and he also demystified friction, opening the way for its study. Such study though, on the nature of friction, was not to be undertaken for several decades.

It was the growing realization of the financial impact of energy losses and the technological limitations that friction imposed that brought its study back to the foreground. Indeed, in his 1734 treatise supporting his patent for disc bearings, Jacob Rowe was probably the first to quantify the expected savings from the adoption of a tribological device. He estimated a grand total of £947,500 per annum for the whole Kingdom of Great Britain, a notable amount for that time. Rowe's intuition on the nature of friction was arguably lacking, but that was not the case with Robert Hooke. The latter presented a discourse on carriages at the Royal Society in 1685. In it, and while discussing the rolling friction on the wheels of a vehicle, he showed great intuition by recognizing the two components of friction, namely surface deformation and adhesion. With regard to surface deformation, he was keen to argue that it was only plastic deformation that would cause power loss. Unfortunately, when it came to adhesion, he only considered it at the back of the wheel, therefore distorting its effect.

If the Royal Society had the privilege of Robert Hooke's insights on friction, it was to its French counterpart (the Academie Royale) that the first focused study of the phenomenon was submitted. Motivated by the increasing dependence of society on machines and noticing the dearth of attention to friction, a factor so crucial to their operation, Guillaume Amontons presented his paper on the subject on December 19, 1699. In that paper, he described a set of careful experiments that led to the two laws that bear his name:

- Friction is proportional to the applied weight
- Friction is independent of the contact area

It should be noted here that these two laws are generally valid for dry friction, but Amontons actually coated the contact surfaces with aged pork fat. It was probably this coating that led him to also measure a constant coefficient of friction of approximately 1/3, regardless of the pair of materials tested (copper, iron, lead and wood in different combinations). The notion that friction is independent of the contact area between materials was unorthodox enough that Amontons felt compelled to ponder the underlying mechanism responsible for it. He disregarded adhesion, which would be inconsistent with the second law, and focused instead on the roughness of the surfaces. He proposed that this is due to protuberances (asperities) that interlock when surfaces are brought to contact. Therefore, friction is the force needed to repeatedly raise the irregularities of one surface over those of the other, to allow relative motion. If the asperities are elastic, a similar force is required to deform them enough to clear a path for each other. Both of these mechanisms are consistent with a surface independent frictional force. As Amontons had anticipated, his work was met with skepticism, and Philippe de la Hire took it upon himself to confirm his results. He promptly did so, and he also extended Amontons' proposed physical mechanism, by admitting the possibility that some of the asperities be broken to allow the relative motion. In this way, he introduced shearing and the resulting permanent deformations to the study of friction, although he did realize that such a source of resistance would be surface size dependent. The theory of rigid interlocking asperities opened a clear path to the calculation of the relationship between surface properties and friction. The mathematician Antoine Parent noted that, if surface irregularities were to be considered slopes of fixed inclination α, then the coefficient of friction would be $\tan\alpha$. A more complicated surface model, and one that introduced the most popular asperity model since, was studied by Bernard Forrester de Belidor in 1737. He considered each surface to be covered by close packed hemispherical asperities. The results of his calculations for such two surfaces in contact agreed with both of Amontons' laws and yielded a value for the coefficient of friction, of ~ 0.35.

Back in Britain, John Theophilus Desaguliers, made the first tentative steps toward including cohesion and adhesion in the theory of friction. In 1725 he had presented a paper to the Royal Society, including experiments where spheres of lead were brought together and cold welded by means of hand pressure. A series of lectures culminated in his 1734 book, *A course of Experimental Philosophy.* In it, although he accepts Amontons' results and theory, he warns that friction may actually rise for well polished surfaces, since the "Attraction of Cohesion" becomes significant as the surfaces come closer.

Up to the middle of the 18th century, the distinction between static and kinetic friction did not exist. It was Leonhard Euler in 1748, who first noticed the difference. In a paper submitted to the Academy of Sciences in Berlin he set out to calculate the influence of friction upon the static equilibrium and motion of bodies on an inclined plane. In the course of his calculations, he introduced the symbol μ for the coefficient of friction and found the limiting angle for motion to commence. He did observe though, that the motion thus started is uniformly accelerated, indicating a larger coefficient of static friction, compared to that of kinetic friction.

Near the end of the 18th century, the industrial revolution was under way as was the naval competition of the great powers. The struggle of the French navy prompted the Paris Academy of Sciences to offer prizes, for scientific work on relevant problems. Charles Augustin Coulomb was the winner of two such prizes, the first one for the improvement of naval compasses, the second one for his research on friction. Coulomb's experimental apparatus was not fundamentally different from Amontons'. Several factors set Coulomb's work apart though. He studied the effect of more parameters on friction. He examined each of these parameters, in a range that mirrored realistic applications. He strove to fit his data with empirical equations and he elegantly extended earlier work, to explain his experimental observations. To the previously explored variables of load and surface area, Coulomb added speed and time of repose (the time of resting contact between the surfaces). The effect of the time of repose had been noted in practice, but Coulomb studied it in detail and was able to use his results to find a general fitting equation for it. The choice of materials he experimented with was focused mainly on maritime applications and he experimented with both clean and lubricated surfaces, studying separately the commonly used lubricants of the time.

Aware of previous work on adhesion and cohesion, Coulomb made sure not to dismiss the effect. In fitting his friction (F) versus load (P) data, he wrote an equation of the form:

$$F = A + \mu P \tag{1.1}$$

were A is the contribution due to adhesion or cohesion, while μP is the contribution due to interlocking asperities. This form is still in use today. Given that the experiments showed no dependence of friction on apparent contact area (which should affect A) and that the fits of eq. (1.1) to the data gave very small values for A, Coulomb deduced that the effect of adhesion or cohesion was not significant.

Regarding the effect of relative velocity on friction, the difference between static and kinetic friction was noted and the general observation that this was large for fibrous materials and minuscule for metals was made. Coulomb is also credited with a third law of friction, claiming that:

- Friction is independent of the relative velocity of the surfaces

In reality, Coulomb made that claim for contacts of similar materials (wood-on-wood or metal-on-metal) noting in his data the exception of wood-on-metal, where kinetic friction increased with speed.

With respect to the nature of friction, the rigid asperities theory seemed to explain all but the time of repose results of his experiments. To address this issue, Coulomb noted that the effect is pronounced only when fibrous surfaces (such as wood) are involved. He employed the brush-bristle analogy, first introduced by

Musschenbroek, for these surfaces. The asperities in this case are flexible bristles, that slowly tangle, as the materials are pressed in contact, yielding a time-increasing coefficient of static friction. When motion is initiated, the bristles on each surface are bent onto each other, thus filling the vacuums between them and preventing further entanglement. By this compacting, they also create an irregular surface, the rigid asperities of which interlock with those of the opposite face, per the earlier theories.

In his work, Coulomb crystallized the basic knowledge with which engineers were to work until the early 20th century, with respect to sliding friction. People like George Rennie in England and Arthur Jules Morin in France were to expand the range of his experiments to other materials and confirm his results. In terms of the fundamental mechanisms of friction though, the technology to explore them in more detail was simply not available.

The picture was of course far from perfect and John Leslie, in the beginning of the 19th century, raised two important issues with it. Regarding the interlocking, rigid asperities mechanism, he pointed out that such protuberances would have to present an average symmetry in all directions of the surface plane. That meant though, that the work expended during the upslope motion of each asperity would be recovered on the downslope motion, yielding a null net effect. Regarding the cohesion/adhesion mechanism, he noted that, for horizontal surfaces, normal forces would perform no work and have no effect on motion. He extended the argument to irregular surfaces, by noting that, on average, there should be as many contact points where the sliding surface would be pulled backwards as forward. His proposal then was that the surface topography at a contact continuously changes, as a result of the loading. specifically, he suggested that, as the asperities of one surface are raised up the asperities of the other the load makes them crumble. Therefore, the downslope part of the motion is eliminated, causing the loss of power. In this way, he amended the interlocking asperities mechanism, but he also brought attention to the concept of surface deformation at the microscopic level of individual asperities.

For the rest of the nineteenth century, tribological developments centered on lubrication, spurred by the commercialization of mineral oil. On the other hand, the tools of linear elasticity and contact mechanics, that were introduced by Augustin Louis Cauchy and Heinrich Hertz respectively, provided solid foundations for the modern understanding of friction.

1.3 20th Century Friction

The confluence of new, more precise surface imaging techniques and a better understanding of matter, both in bulk and in its components, removed several layers of speculation with regards to the mechanisms of friction in the 20th century. Profilometry and microscopic observation of sections revealed roughness and height variations of order 100-1000Å for polished surfaces. Meanwhile, the experimental and theoretical studies in atomic physics have set the scale for interatomic interaction ranges to a few Angstroms. Load bearing between two materials in contact then occurs over a very limited area, at the tips of their asperities, as shown schematically in Figure 1.2.

Following the landmark work of Bowden and Tabor[8], one can use continuum mechanics as a first order tool to study these contacts. Such analysis indicates that, at those contact points, the elastic limits of the materials are very quickly surpassed. Plastic flow of the weaker material leads to irreversible deformation and the increase

Figure 1.2: Microscopic structure of contact surfaces

of the contact area, until the pressure equals the yield strength of that material:

$$A = \frac{1}{p_m} P \tag{1.2}$$

where A is the real area, P is the loading force and p_m is the average asperity yield strength at the contact surface. Even on account of this flattening of the asperities, there is a large discrepancy between the apparent and real area of contact between two objects. For instance, consider two flat surfaces of apparent contact area 1cm^2 in contact. For a typical metal yield strength of order 1GPa, the real contact area between them will only be approximately 1/10,000th of the apparent area for a load of 1kg ($\sim$ 10N).

The realization that the real contact area between materials varies with the load cast Amontons' laws in a whole new light. The independence of the coefficient of friction from the applied normal force (over a wide range at least) still stands, but the independence of the frictional force from the surface area clearly no longer does. Thus, the "onerous" dependence of adhesive and cohesive forces on the area of contact, that made earlier researchers question the contribution of these interactions to friction, is no longer a problem. Quite the opposite in fact. For a uniform surface, Bowden and Tabor proposed and demonstrated, that such forces would be proportional to the real area of contact:

$$S = sA \tag{1.3}$$

where s is a suitable coefficient of proportionality. Equations (1.2) and (1.3) yield:

$$\mu_s = \frac{S}{P} = \frac{s}{p_m} \tag{1.4}$$

which is indeed independent of the load.

Focusing on metals, they performed classic experiments to isolate and study the relative contributions to frictional force of shearing and ploughing. The latter refers to the displacement of softer material in the path of motion of a harder asperity, that has penetrated it. They found that the shearing forces dominate and that it is the parameters of the weaker metal that determine the coefficient of friction in a pair, per eq. (1.4). As far as the dynamics of the sliding are concerned, direct observation is extremely difficult. However, through careful analysis of the tracks left behind after sliding, they were able to make some very astute observations. The role of adhesion was confirmed by evidence of cold welding. Furthermore, shearing was predominantly found to take place in the softer material, consistent with the work hardening expected at the contact, and the role of the strength of that material in the determination of the friction coefficient.

If a qualitative picture has been formed by the work of Bowden and Tabor, the missing dynamic details are required for the empirical factors to be connected systematically to material properties. The advent of powerful computers provided science with a new tool to bridge theory and experiment and to examine the minutiae of processes that can only be recorded as statistical averages in the physical world. The contact problem in particular can be approached computationally, through either continuum mechanics or atomistic simulations. Continuum simulations treat the material as a bulk with smooth boundaries. Atomistic simulations capture the discrete nature of a material, treating each of its atoms individually. The computational cost of such a treatment is much higher than in the continuum case. In the case of asperities though, where the characteristic dimensions (10-100Å) are only an order or two of magnitude larger than typical interatomic distances, atomic structure can lead to drastic departures from continuum theory predictions, as shown by Luan and Robbins[18]. Realistic atomistic simulations, of systems as large as a typical asperity, only became practical in the last two decades. Some of the most interesting work in the field has been performed by the groups of Mark Robbins and Donald Brenner. The former group has been focusing more on fundamental, qualitative comparisons of continuum and atomistic simulations, the deficiencies of continuum theories, when dealing with the atomic scale roughness of contacts, and the implications of such shortcomings in the interpretation of Atomic Force Microscopy (AFM) friction experiments[18, 19]. From our perspective, their most important result is that, depending on the atomic scale surface roughness of an asperity, continuum calculations may be off in estimating the work of adhesion, stresses and contact area by a factor of order one, but may be orders of magnitude off with respect to friction. Brenner's group has been working in parallel to ours. Their experiments focus on the quantitative study of realistic Al-Cu contacts[15] and the effects of Joule heating[22] on them. We are using a different MD code and, by taking a more fundamental approach to electrodynamics, we allow a wider range of relevant effects to be studied, beyond Joule heating. Their results do provide an important reference.

Chapter 2

Implementation

2.1 Overview

In deciding to design a numerical experiment on friction, we need to seek the basic unit of material contact. We now know that, with few exceptions (e.g. mica), it is exceedingly difficult to prepare atomically flat surfaces. Features of sizes starting at tens to hundreds of Angstroms characterize the roughness of even well polished surfaces. Scientists since Amontons have assumed the existence of such asperities but they were only seen in the beginning of the 20th century. Contrary to the prevalent ideas till then, these asperities are not tightly interlocking between materials and it is in fact their tips that are the mediators of load between contacting surfaces. This is a consequence of both the irregularity of shape of those asperities and the short range of atomic potentials. The simple Lennard-Jones potential for instance is usually used with a cut-off of approximately $2.2r_c$, where r_c the equilibrium distance for a pair of atoms, typically between 3Å and 5Å.

With our focus on the asperity tips then, the simplest realistic system we can use to study sliding, is that of a hemispherical asperity sliding on a flat surface. The

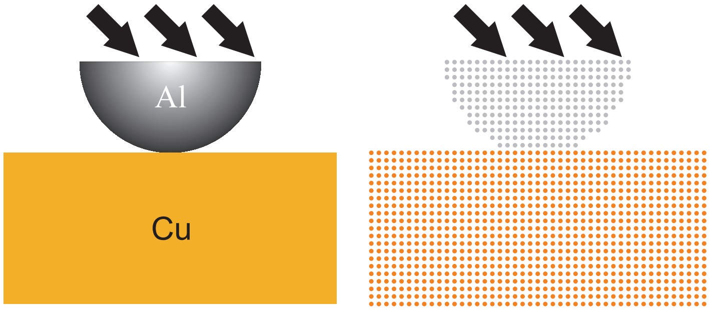

(a) Continuum view (b) Atomic view

Figure 2.1: The simulated system

hemispherical approximation for the asperities goes back to the 18th century studies of Bernard Forrester de Belidor. The particular configuration, of a hemispherical slider on a flat surface, is regularly used in physical friction experiments, allowing a closer correspondence between such experiments and our numerical studies. That correspondence is not perfect, as the surfaces of our objects are dry and clean for the reported simulations and both objects start as perfect monocrystals. Typical engineering metals usually have polycrystalline structure and their surface readily develops an oxide layer, which has been shown by Bowden and Tabor to be a crucial moderating factor of adhesion.

A schematic illustration of the configuration of our experiment then is shown in Figure 2.1. The figure illustrates the difference between the two methods that are typically used to study materials and their mechanical behavior. In the continuum approach (Figure 2.1(a)), the parts of our system would have well defined, smooth boundaries. These would be enclosing volume elements, characterized homogeneously by their bulk elastic and plastic properties. A suitable potential would describe the interaction between the different materials and provide the surface stresses on each. These stresses, as well as the stresses between adjacent volume elements of the same material, would dictate the evolution of each volume element and the system as a whole. In the atomistic approach (Figure 2.1(b)), which is the one we utilize, the parts of our system are defined by their atoms, and the macroscopic behavior is a product of the individual interactions between the latter. The continuum view is computationally advantageous, owing to the simpler theory of plasticity and linear elasticity employed in the calculations and the fact that the discretization of the system can be non-uniform, with volume element size dependent on the dynamic complexity of a particular area. The atomistic view leads to more costly simulations, most obviously because of the increase in the number of computational elements, but also because of the complex nature of the atomic interactions. This computational expense is justified, when one considers the drastic qualitative and quantitative departures from the continuum predictions that are introduced by the atomic scale surface structure and roughness in systems of this size, as shown by Luan and Robbins[18, 19].

To study the dynamics of the system, we need to set it in motion and measure the attendant coefficient of friction. We establish sliding by holding the bottom of the lower surface fixed and rigidly translating the top of the slider. The horizontal translation velocity is held constant. The normal velocity may be null, or determined by a feedback loop, which targets a prescribed normal force between the two objects. By measuring the reactive force to the imposed motion of the top of the slider, we can use its horizontal and normal components, to calculate the coefficient of friction. Measurement of the static coefficient of friction is also possible, if we start moving the slider top after a contact and the prescribed normal force have been established. The static coefficient of friction can then be found, as the peak of our coefficient of friction vs. time graph.

The electrodynamic aspects of our simulation are introduced through the application of a potential difference between the top of the slider and the bottom of the lower surface. The resultant current flows according to the distribution of conductivity in the cells of the computational volume. That distribution in turn reflects the density of the atom species present at each cell. On the other hand, the heat resulting from the current flow at each cell is added as kinetic energy to the relevant atoms. The metal atoms are also considered stripped of their valence electrons, and respond to local electromagnetic fields, due to their positive charge.

Two main tools are required, to perform the study outlined above. The first is a proper atomic potential, to perform the calculations of atomic interactions inside and between the materials forming the contact. The second is a scheme for calculating the electric currents and fields within the simulation volume, given externally imposed boundary conditions. These two tools have to be meshed in an efficient numerical code, so that the results of one inform the calculations of the other and meaningful data are produced in reasonable amounts of time.

Our application did pose some important requirements for the selection of an atomic potential. The potential had to be general enough so that not only different metals could be described with the same formulation, but also potentially impurities and surface oxides for later experimentation. The mere fact that we were going to study surfaces also limited our choices, as the potential needed to allow proper behavior and not just extend bulk properties there. The issue of computational practicality cannot be underestimated in such a study. While Density Functional Theory has been used to produce more quantum-mechanically sound simulations of small systems, such as molecules, such an approach in an application involving hundreds of thousands to millions of atoms was simply untenable. Our focus then had to be shifted to semi-empirical potentials. The magnitude of the problem can be illustrated by the fact that even the latter, simpler methods, currently take $\sim$ 1ms/particle/time step and make meaningful simulations run for days on clusters of tens of processors.

The electrodynamics scheme was developed from scratch. The obvious first choice for performing such calculations was to solve the full set of Maxwell equations. Indeed, after some research, Yee's elegant scheme came to our attention and an implementation of it was tried. The most important issue with such an approach was the large discrepancy between the time steps for molecular dynamics and electrodynamics. Adopting the faster time step for both was not an option as it would make our simulations impractical. We overcame this problem, by viewing electrodynamics as a series of steady states, corresponding to the successive atomic configurations of our system. The calculation of these steady states is through a much faster iterative process.

2.2 Atomic Potential

The selection of an atomic potential did not take long. The Modified Embedded Atom Method (MEAM) had been employed in previous simulations of our group, while it did seem to satisfy the requirements of generality and efficiency for the project at hand. The pre-existing MEAM code was single-species only, so work was needed to generalize the potential for a multi-species application. The constant evolution of the MEAM formalism can be traced through the relevant papers published since its introduction (see for instance [9, 11, 3, 4, 6, 17, 30, 14] for a list of relevant papers). Such evolution did not always increase the general accuracy of the potential as much as optimized it for the particular problem at hand. We had therefore some options available, when considering the form of MEAM to be put in code. In anticipation of possible pitfalls and after the inevitable trial and error, we picked what we felt was the most appropriate formulation.

More testing demonstrated that the multi-species MEAM could not be successfully employed between separated pieces of material. The current version of the code uses a combination of the MEAM potential for intra-species calculations and the much simpler Rose potential for inter-species calculations. The contributions $E_{M,tot}$ and $E_{R,tot}$ respectively, from the two potentials to the energy of our system, are independent. Therefore, the total potential energy of the system is:

$$E_{tot} = E_{M,tot} + E_{R,tot}$$

In what follows, we will describe these two contributions to the total potential of the system. The force on particle m due to the atomic potential will be calculated from the analytical form derived from the definition:

$$\vec{f}_m = \frac{dE_{tot}}{d\vec{R}_m}$$

This is a long, if straightforward, derivation, that can be found in the appendix (cf. Appendix A).

2.2.1 Rose potential

Rose et al. introduced an equation of state[25, 26] to describe the evident universality of form for the binding energies of bulk metals and bimetallic contacts. While a simpler, pairwise potential compared to MEAM then, it is well suited to approximate the interaction of the clean metallic surfaces. From a coding point of view, the Rose potential is employed by MEAM in the calculation of reference crystalline structure values, allowing a smoother implementation of the tandem Rose-MEAM scheme. The general formulation, ascribes a potential energy:

$$E = -E_c \left(1 + a^*\right) e^{-a^*} \tag{2.1}$$

per atom, with:

$$a^* = \alpha \left(R/r_e - 1\right) \tag{2.2}$$

Here, E_c is the energy corresponding to the equilibrium distance r_e between neighboring atoms in a bulk or between two metallic surfaces and α is a suitable fitting parameter. R is the actual distance corresponding to r_e.

In our case, we will use this potential as a pairwise atomic potential between atoms of different species. It will provide a contribution:

$$E_{R,tot} = \sum_i E_{R,i} \tag{2.3}$$

to the total energy of our system, where:

$$E_{R,i} = \sum_{j(species(j) \neq species(i))} S_{ij} E_{R,ij} \tag{2.4}$$

The factor S_{ij} describes the screening effect that other neighbors may have on the interaction of atoms i and j. We will elaborate on this issue later (cf. section 2.2.3).

2.2.2 MEAM

The Embedded Atom Method (EAM) was introduced by Daw and Baskes[9] as a semi-empirical potential based on Density Functional Theory (DFT) theorems. The basic DFT footing for EAM is the finding that the potential energy for adding an impurity to an atomic system is a functional of the electron density distribution of the unperturbed system. By viewing each atom in a system as an impurity to the rest of the system, Daw and Baskes built a potential, where the contribution of each atom i to the energy of the system can be quantified:

$$E_{M,tot} = \sum_i E_{M,i} \tag{2.5}$$

and is the sum of two terms. One is a pairwise potential, capturing nuclei-nuclei interaction. The other is an embedding term, dependent on the species of the "impurity" and an effective "electron density" projected onto its location from its neighbors:

$$E_{M,i} = F_i(\bar{\rho}_i) + \frac{1}{2} \sum_{j(\neq i)} S_{ij} \Phi_{ij}(R_{ij}) \tag{2.6}$$

Here, F_i is the embedding energy of atom i in local background charge density $\bar{\rho}_i$, Φ_{ij} is the pair potential between atoms i and j and, as in eq. (2.4), S_{ij} is a screening function which introduces the modulation of the direct effects of atom j on atom i, due to the presence of all other atoms (cf. section 2.2.3). One of the most important practical advantages of EAM is that it is not bulk limited. Because all the quantities involved can be defined throughout the extent of a finite piece of material, it can be applied to study surface phenomena. Indeed, the reproduction of proper surface relaxations was one of the qualifying tests for the potential[11].

The transition to the Modified Embedded Atom Method (MEAM)[2, 5], sought to expand the repertoire of EAM, which had mainly been applied to metals and their impurities. The main departure was in the calculation of the background charge density $\bar{\rho}_i$. In EAM, this was just a linear superposition of spherically symmetric terms from each neighbor. MEAM introduced angular dependencies, to capture the nature of a broader array of bonds. The implementation of these angular dependencies varied in details over the years of development and with respect to specific applications[11, 3, 4, 6, 17, 30, 14]. In what follows, we will present the specific formulation for MEAM that we have utilized in our code.

The general form for the embedding function in MEAM is:

$$F_i(\bar{\rho}_i) = A_i E_{c,i} \left(\frac{\bar{\rho}_i}{\bar{\rho}_i^0} \right) \ln \left(\frac{\bar{\rho}_i}{\bar{\rho}_i^0} \right) \tag{2.7}$$

where A_i is an adjustable parameter, while $\bar{\rho}_i^0$ is the background electron density and $E_{c,i}$ the cohesive energy in a species specific, equilibrium reference structure for which these quantities can be determined (e.g. the fcc zero temperature crystal for Al or Cu). The actual background density, $\bar{\rho}_i$, has four components:

$$\rho_i^{(0)} = \sum_{j(\neq i)} S_{ij} \rho_j^{a(0)}(R_{ij}) \tag{2.8}$$

$$\left(\rho_i^{(1)}\right)^2 = \sum_{\alpha} \left[\sum_{j(\neq i)} u_{ij}^{\alpha} S_{ij} \rho_j^{a(1)}(R_{ij}) \right]^2 \tag{2.9}$$

$$\left(\rho_i^{(2)}\right)^2 = \sum_{\alpha,\beta} \left[\sum_{j(\neq i)} u_{ij}^{\alpha} u_{ij}^{\beta} S_{ij} \rho_j^{a(2)}(R_{ij}) \right]^2 - \frac{1}{3} \left[\sum_{j(\neq i)} S_{ij} \rho_j^{a(2)}(R_{ij}) \right]^2 \tag{2.10}$$

$$\left(\rho_i^{(3)}\right)^2 = \sum_{\alpha,\beta,\gamma}\left[\sum_{j(\neq i)} u_{ij}^{\alpha}u_{ij}^{\beta}u_{ij}^{\gamma}S_{ij}\rho_j^{a(3)}(R_{ij})\right]^2 - \frac{3}{5}\sum_{\alpha}\left[\sum_{j(\neq i)} u_{ij}^{\alpha}S_{ij}\rho_j^{a(3)}(R_{ij})\right]^2 \tag{2.11}$$

here $u_{ij}^{\alpha} = \frac{R_{ij}^{\alpha}}{R_{ij}}$ is the α component of the unit vector, $\hat{u}_{ij}$, pointing from atom i to atom j, and:

$$\rho_j^{a(h)}(R) = \rho_{0,j}e^{-\beta_j^{(h)}(R/r_{e,j}-1)} \tag{2.12}$$

$r_{e,j}$ being the nearest neighbor distance in the species specific equilibrium structure referred to earlier. In terms of its components, $\bar{\rho}_i$ is equal to:

$$\bar{\rho}_i = \frac{2\rho_i^{(0)}}{(1+e^{-\Gamma_i})} \tag{2.13}$$

where:

$$\Gamma_i = \sum_{h=1}^{3} t_i^{(h)}\left[\rho_i^{(h)}/\rho_i^{(0)}\right]^2 \tag{2.14}$$

with $\beta_j^{(h)}$ and $t_j^{(h)}$ being species dependent, adjustable parameters, and $t_j^{(0)} = 1$.

The pair potential $\Phi_{ij}(R)$ for a single species system can be approximated by assuming a reference structure for which the energy per atom E_{ij}^{u} is known and solving eq. (2.6) for Φ_{ij}:

$$\Phi(R) = \frac{2}{Z}\left[E^u(R) - F[\bar{\rho}(R)]\right] \tag{2.15}$$

where the indexes ij have been dropped, since there's only one species of atoms. Z is the number of first neighbors in this reference structure. We have assumed interaction with the first neighbors only, a well tested approximation (see [3]). $E^u(R)$ can be determined using the equation of state by Rose et al., per eqns. (2.1) and

(2.2):

$$E^u(R) = -E_c\left(1 + a^*\right)e^{-a^*}$$

with:

$$a^* = \alpha\left(R/r_e - 1\right)$$

According to Baskes, we can write for α:

$$\alpha = \sqrt{\frac{9\Omega B}{E_c}} \tag{2.16}$$

where E_c, Ω and B are the cohesive energy, atomic volume and bulk modulus for the reference structure, at its equilibrium state, when the first neighbor distance is r_e.

Determining a pair potential for inter-species interaction is more involved. Following the work in reference [3], we will assume that the particular geometry of a structure enters our calculations only through the distribution of electronic charge and atomic screening effects while the pair potential between two species does not depend on it. Then, we can assume a cubic crystal of two species of atoms, in equal proportions and in such a configuration that the nearest neighbors of each atom belong to the other species. Additionally we will require that each atom is a center of symmetry for the crystal, to simplify electron density calculations. For such a system, the average energy per atom is:

$$E^u_{ij}(R) = \frac{1}{2}\left[F_i\left(Z_{ij}\rho_j^{a(0)}(R)\right) + F_j\left(Z_{ij}\rho_i^{a(0)}(R)\right) + Z_{ij}\Phi_{ij}(R)\right]$$

where Z_{ij} and R are the number and distance of nearest neighbors in our structure.

As before, we can solve this equation for Φ_{ij}:

$$\Phi_{ij}(R) = \frac{1}{Z_{ij}} \left[2E^u(R) - F_i \left(Z_{ij} \rho_j^{a(0)}(R) \right) - F_j \left(Z_{ij} \rho_i^{a(0)}(R) \right) \right] \tag{2.17}$$

E^u_{ij} can again be calculated by an equation of state of the form of eq. (2.1). The equilibrium state here may not be known. A first estimate for the nearest neighbor distance though could be given by an r_e corresponding to an atomic volume of:

$$\Omega = \left(\frac{\Omega_i + \Omega_j}{2} \right) \tag{2.18}$$

With the aid of this estimate, the actual r_e, as well as the two adjustable parameters E_c and α can be determined given three independent (i.e. corresponding to different inter-atomic distances), ab-initio calculations of the energy E^u_{ij}.

2.2.3 Screening

To limit the extent of interactions in a smooth fashion, as well as to determine the effect of neighboring atoms on pairwise interactions, we have multiplied both the electron density and the pairwise potential by a screening function:

$$S_{ij} = \prod_{k(\neq i,j)} S_{ikj} \tag{2.19}$$

S_{ikj} quantifies the shielding that atom k imposes on the pairwise interaction between atoms i and j. This is achieved through a simple geometrical argument. Specifically, let us consider the ellipse passing through all three atoms. In a Cartesian coordinate system concentric with it and so aligned that the two atoms i and j are lying on the x axis, the equation of the ellipse is:

$$x^2 + \frac{y^2}{C_{ikj}} = \left(\frac{1}{2}R_{ij}\right)^2$$

where:

$$C_{ikj} = \frac{2\left(X_{ik} + X_{kj}\right) - \left(X_{ik} - X_{kj}\right)^2 - 1}{1 - \left(X_{ik} - X_{kj}\right)^2} \tag{2.20}$$

with:

$$X_{ik} = \left(\frac{R_{ik}}{R_{ij}}\right)^2 \tag{2.21}$$

and, similarly:

$$X_{kj} = \left(\frac{R_{kj}}{R_{ij}}\right)^2 \tag{2.22}$$

C_{ikj} is therefore a measure of the extent of the ellipse in the y direction. We expect then that the screening effected by particle k will be stronger for smaller values of C_{ikj} and will fall off gradually as C_{ikj} increases. In fact, we assume that the screening is complete ($S_{ikj} = 0$) for $C_{ikj} < C_{min,ikj}$ and it falls off in a continuous manner to allow a fully unaffected interaction ($S_{ikj} = 1$) for $C_{ikj} > C_{max,ikj}$. In mathematical language:

$$S_{ikj} = g_c(x_{ikj}) = g_c\left(\frac{C_{ikj} - C_{min,ikj}}{C_{max,ikj} - C_{min,ikj}}\right) \tag{2.23}$$

the cutoff function g_c being:

$$g_c(x_{ikj}) = \begin{cases} 1 & x_{ikj} \geq 1 \\ \left[1 - (1 - x_{ikj})^4\right]^2 & 0 < x_{ikj} < 1 \\ 0 & x_{ikj} \leq 0 \end{cases} \tag{2.24}$$

$C_{max,ikj}$ and $C_{min,ikj}$ are parameters that most generally depend on the species of atoms i, k and j, modulo the exchange symmetry between i and j.

2.3 Electrodynamics

We need to deal with the issue of charge mobility in our simulation, so as to study the effects of currents in the friction between metallic surfaces. To do that we consider two components of charge and current. One component is due to the valence electrons. These are considered independent from the "donor" atoms and treated as a bulk, through the corresponding charge and current densities. The other component is due to the atoms themselves, positively ionized due to the "loss" of their valence electrons. These are treated individually by the code. For the calculation of the electromagnetic fields though, their contributions are averaged into the appropriate charge and current densities. The electromagnetic fields, as well as the charge and current densities are calculated over a static rectangular grid, spanning the simulated volume.

2.3.1 Electromagnetic Field Evolution

In solving any electromagnetic problem, the most basic starting point is the set of the four Maxwell equations:

$$\frac{\partial \vec{E}}{\partial t} = c^2 \left(\nabla \times \vec{B} - \mu_0 \vec{J} \right) \tag{2.25}$$

$$\frac{\partial \vec{B}}{\partial t} = -\nabla \times \vec{E} \tag{2.26}$$

$$\nabla \cdot \vec{B} = 0 \tag{2.27}$$

and:

$$\nabla \cdot \vec{E} = \frac{\rho}{\epsilon_0} \tag{2.28}$$

$\vec{E}$ and $\vec{B}$ are the electric and magnetic field respectively in the simulation volume. Atoms and their valence electrons provide separate contributions to the charge density:

$$\rho = \rho_e + \rho_a \tag{2.29}$$

and the current density:

$$\vec{J} = \vec{J}_e + \vec{J}_a \tag{2.30}$$

The last two of the Maxwell equations (eqs. (2.27) and (2.28)) are actually not independent equations. Instead, they provide initial conditions, which are therefore preserved by the other two equations, and the conservation of charge:

$$\frac{\partial \rho}{\partial t} = -\nabla \cdot \vec{J} \tag{2.31}$$

Indeed, taking the divergence of eq. (2.27), we have:

$$\frac{\partial}{\partial t}\left(\nabla \cdot \vec{B}\right) = -\nabla \cdot \left(\nabla \times \vec{E}\right) = 0$$

and, from the divergence of eq. (2.25):

$$\frac{\partial}{\partial t}\left(\nabla \cdot \vec{E}\right) = c^2\left[\nabla \cdot \left(\nabla \times \vec{B}\right) - \mu_0 \nabla \cdot \vec{J}\right] = c^2 \mu_0 \dot{\rho} \Rightarrow$$

$$\frac{\partial}{\partial t}\left(\nabla \cdot \vec{E} - \frac{\rho}{\epsilon_0}\right) = 0$$

We will therefore have to be careful to set up physically plausible systems, but we cannot extract useful dynamic information from these two equations during our simulations.

The system we are left with is that of equations (2.25), (2.26) and (2.31).

Taking into account the vector components of $\vec{E}$, $\vec{B}$, and $\vec{J}$ this is a system of 7 equations and 10 unknowns. We will resolve this issue by adding an equation of motion for the electronic current density and by calculating the atomic current density using the relevant particle velocities calculated by molecular dynamics.

2.3.2 Charge and Current Density Evolution

2.3.2.1 Electrons

Tracking electrons in our classical simulation poses two important difficulties. The first one is in terms of the physical validity of such an effort. Electron wavelengths are comparable to the inter-atomic distances in a crystal and treating them as point charges is at least debatable. The second one is in terms of computational complexity. Even if one tracks only valence electrons, the number of particles in the simulation increases and so do storage requirements and computation time. The problem is exacerbated by the small mass of the electrons, which dictates time steps much smaller than those necessary for purely atomic simulations. The first difficulty cannot be easily addressed within the classical framework. We will still use the particle picture to motivate our solution and allow our results to justify the prudence of such a choice. We will attempt to tackle the second difficulty by considering an electron "fluid", rather than individual electrons. This fluid will comprise of only the valence electrons and will be tracked through the charge density it projects at each grid point. The rest of the electrons will be considered bound to their respective nuclei.

Charge Density The initial charge density configuration can be found by starting with the system at an equilibrium configuration, with no electromagnetic forces or fields acting on it. Under such conditions, taking the electron charge density to be equal in magnitude and opposite in sign to the ionic charge density should be a good approximation. From there on, we can let the electron charge density evolve in response to atomic movement and external fields. The evolution of the electron charge density will be governed by the total current flowing into a grid point n through the charge conservation equation:

$$\dot{\rho}_{e,n} = -(\vec{\nabla} \cdot \vec{J}_e)_n \tag{2.32}$$

Current Density To find the equation of evolution of the current density, we will start with the equation of motion of individual electrons:

$$m_e \frac{d\vec{v}}{dt} + \gamma q_e \vec{v} = q_e \vec{E} + q_e \vec{v} \times \vec{B} \tag{2.33}$$

The second term on the left hand side imposes a terminal speed for the electron. In this way, we recover Ohm's law. The latter dictates the value of the factor γ. We will come back to this issue later. For now, we will multiply eq. (2.33) by n_e, the numerical density of electrons, to obtain:

$$\frac{m_e \rho_e}{q_e} \frac{d\vec{v}}{dt} + \gamma \vec{J}_e = \rho_e \vec{E} + \vec{J}_e \times \vec{B}$$

but,

$$\frac{d\vec{J}_e}{dt} = \frac{d}{dt}\left(\rho_e \vec{v}\right) = \dot{\rho}_e \vec{v} + \rho_e \frac{d\vec{v}}{dt}$$

Since charge cannot be spontaneously generated or destroyed, $\dot{\rho}_e = 0$. Therefore:

$$\frac{d\vec{J}_{e,n}}{dt} = \frac{q_e}{m_e}\left(\rho_{e,n}\vec{E}_n + \vec{J}_{e,n} \times \vec{B}_n - \gamma_n \vec{J}_{e,n}\right) \tag{2.34}$$

where the n index is a reference to the grid point of interest.

γ-factor As mentioned above, the value for γ in eq. (2.33) is dictated by Ohm's law. Indeed, according to eq. (2.34), for $B = 0$, the electron terminal current will be:

$$\vec{J}_{e,n} = \frac{\rho_{e,n}\vec{E}_n}{\gamma_n}$$

and it has to satisfy:

$$\vec{J}_{e,n} = \frac{\rho_{e,n}\vec{E}_n}{\gamma_n} = \sigma_n \vec{E}_n \Rightarrow$$

$$\gamma_n = \frac{\rho_{e,n}}{\sigma_n} \tag{2.35}$$

where σ is the conductivity of the surrounding material. The γ value from eq. (2.35) can be expected to be valid even when $B \neq 0$, as long as the electron cyclotron frequency ($\omega_{c,e} = q_e B/m_e$) is smaller than the frequency of our time steps.

The conductivity value σ will depend on the composition and density of the atomic environment around a grid point. To take these effects into account, we will write:

$$\sigma = \sum_s \frac{\rho_s}{\rho_{s,0}} \sigma_s \tag{2.36}$$

where the sum is over the atom species in the cell around grid point n. ρ_s is the ion charge density due to species s. σ_s is the conductivity of species s at its reference density $\rho_{s,0}$. In physical terms, eq. (2.36) expresses the assumption, that the different ion species in a cell make independent contributions to conductivity, according to the strengths of the respective populations. Summing the conductivities is equivalent to treating them as connected in parallel, the idea here being that, in a cell with a mixture of materials each one offers an individual path for the current.

Instant Electron Response We will simplify the problem at hand by assuming that the electronic current density responds instantly to field changes, so that:

$$\frac{d\vec{j}}{dt} = \frac{q_e}{m_e}\left(\rho_{e,n}\vec{E}_n + \vec{J}_{e,n} \times \vec{B}_n - \gamma_n \vec{J}_{e,n}\right) = 0 \tag{2.37}$$

Under this assumption, eq. (2.34) becomes a constitutive relation for the current. It can be treated as a system of linear equations, in the components of $\vec{J}$.

2.3.2.2 Atoms

Since the position and velocity of each atom is tracked by the code, there's no need to write ionic charge and current density evolution equations. We will therefore only concern ourselves with writing down expressions for the instantaneous values of these quantities at each grid point.

Charge Density The ionic charge density at a grid point n will be the weighted sum of atomic contributions:

$$\rho_{i,n} = \frac{1}{V}\sum_k w_{n,k} q_k \tag{2.38}$$

where the sum is over the particles belonging to the grid point and its neighbors, V is the cell volume around each grid point and $w_{n.k}$ is a weight function. Originally, the latter was a binary function of whether the particle is located within the confines of cell n. When numerical instabilities were encountered in our attempt to solve the full Maxwell problem, the sudden changes of the ionic charge when particles crossed the boundaries of their cells became prime suspects. A new function was thus adopted, which spreads the ionic charge among neighboring cells:

$$w_{n,k} = \begin{cases} 0 & d_\alpha < |R_n^\alpha - R_k^\alpha| \\ \prod_\alpha \frac{d_\alpha - |R_n^\alpha - R_k^\alpha|}{d_\alpha} & d_\alpha \geq |R_n^\alpha - R_k^\alpha| \end{cases} \tag{2.39}$$

The constants d_α represent the grid point spacings in each direction α. R_n^α and R_k^α are the coordinates of grid point n and particle k respectively.

Current Density The ionic current density will similarly be:

$$\vec{J}_{i,n} = \sum_k w_{n,k} \frac{q_k \vec{v}_k}{V} = \frac{1}{V} \sum_k w_{n,k} q_k \vec{v}_k \tag{2.40}$$

where, again, the sum is over the particles belonging to the grid point and its neighbors.

2.3.3 Numerical Implementation - Attempted Full Problem Solution

In our original approach to the electrodynamic problem, we attempted to implement a full time-domain solver. The realization of the efficiency issues we would be facing, as well as unresolved instabilities in our implementation, convinced us to abandon this scheme. We do describe it here for completeness, and because it was an educational exercise.

2.3.3.1 Scaling

To facilitate the numerical solution of our problem, we need to appropriately scale the physical quantities involved, to eliminate order of magnitude differences between them. To do that we will write each quantity as the product of a scaling factor and a dimensionless variable. For example, we will write:

$$\rho = \rho_0 \rho_d$$

where ρ_d is now a dimensionless variable. The system of equations to be solved now becomes:

$$\frac{\partial \vec{E}_d}{\partial t_d} = \frac{t_0 c^2}{E_0} \left(\frac{B_0}{L_0} \nabla_d \times \vec{B}_d - \mu_0 J_0 \vec{J}_d \right) \tag{2.41}$$

$$\frac{\partial \vec{B}_d}{\partial t_d} = -\frac{t_0 E_0}{L_0 B_0} \nabla_d \times \vec{E}_d \tag{2.42}$$

$$\dot{\rho}_d = -\frac{t_0 J_0}{L_0 \rho_0} \nabla_d \cdot \vec{J}_d \tag{2.43}$$

The ionic component of the current density will be provided by the molecular dynamics. The electronic component though will be provided by eq. (2.37):

$$\rho_d \vec{E}_d = \frac{J_0}{\rho_0 E_0} \left(\rho_0 \tau_0 \tau_d \rho_d \vec{J}_d - B_0 \vec{J}_d \times \vec{B}_d \right) \tag{2.44}$$

We will require that:

$$\left. \begin{array}{c} \frac{t_0 c^2 B_0}{L_0 E_0} = 1 \\ \frac{B_0}{L_0} = \mu_0 J_0 \\ \frac{t_0 E_0}{L_0 B_0} = 1 \\ \frac{t_0 J_0}{L_0 \rho_0} = 1 \\ \rho_0 \tau_0 = B_0 \\ \frac{J_0 \tau_0}{E_0} = 1 \end{array} \right\} \Rightarrow \left\{ \begin{array}{c} \frac{t_0 c^2 B_0}{L_0 E_0} = \frac{t_0^2 c^2}{L_0^2} = 1 \\ \frac{\rho_0 \tau_0}{L_0} = \mu_0 \frac{L_0 \rho_0}{t_0} \\ B_0 = \frac{t_0 E_0}{L_0} \\ J_0 = \frac{L_0 \rho_0}{t_0} \\ B_0 = \rho_0 \tau_0 \\ E_0 = \frac{L_0 \rho_0}{t_0} \tau_0 \end{array} \right\} \Rightarrow \left\{ \begin{array}{c} t_0 = \frac{\tau_0}{\mu_0 c^2} \\ L_0 = \frac{\tau_0}{\mu_0 c} \\ B_0 = \frac{E_0}{c} \\ J_0 = \rho_0 c \\ B_0 = \rho_0 \tau_0 \\ E_0 = \rho_0 c \tau_0 \end{array} \right. \tag{2.45}$$

Using these conditions, we can now write the system of equations to be solved in component form as:

$$\dot{E}_\alpha = \epsilon_{\alpha\beta\gamma}\partial_\beta B_\gamma - J_\alpha \tag{2.46}$$

$$\dot{B}_\alpha = -\epsilon_{\alpha\beta\gamma}\partial_\beta E_\gamma \tag{2.47}$$

$$\dot{\rho} = -\partial_\alpha J_\alpha \tag{2.48}$$

$$\tau\rho J_\alpha - \epsilon_{\alpha\beta\gamma}J_\beta B_\gamma = \gamma J_\alpha - \epsilon_{\alpha\beta\gamma}J_\beta B_\gamma = \rho E_\alpha \tag{2.49}$$

where we are using the Einstein convention and $\epsilon_{\alpha\beta\gamma}$ is the Levi-Civita symbol. The d subscript has been dropped, since all quantities are dimensionless.

The conditions of eqns. (2.45) are all compatible, though only five of them are independent. They allow for two adjustable parameters (in this formulation the resistivity and charge density units) to determine the rest of the scaling factors. Characteristic values for the case of Al are given in table (2.1). Two sets of values are given (first two columns on the table). The first set stems from a calculation of ρ_0, based on 3 valence electrons per atom and a density of $\approx 2.7\text{g/cm}^3$. The second set is based on an experimental estimate of the current density J_0 in a railgun contact, of order of MA/cm^2. In either case, the resistivity of aluminum is taken to be $\approx 2.7 \cdot 10^{-8}\Omega\text{m}$.

Table (2.1) illustrates two problems with our current approach. The first has to do with the time scale, t_0, which is at least four orders of magnitude shorter than the respective scale of molecular dynamics. That is of course the product of the significant disparity, between the characteristic velocities of electromagnetic waves and atomic motion. As a result, for every step of our molecular dynamics simulation, the electromagnetic portion of the code has to perform more than ten thousand steps, with obvious consequences to the computational cost of an already

	$\partial\vec{J}/\partial t = 0$		$\partial\vec{J}/\partial t \neq 0$
t_0 (s)	$2.4 \cdot 10^{-19}$		
L_0 (m)	$7.2 \cdot 10^{-11}$		
τ_0 (Ωm)	$2.7 \cdot 10^{-8}$		
ρ_0 (Cb/m^3)	$2.9 \cdot 10^{10}$	$3.3 \cdot 10^{1}$	$8.8 \cdot 10^{14}$
J_0 (A/m^2)	$8.7 \cdot 10^{18}$	10^{10}	$2.6 \cdot 10^{23}$
E_0 (V/m)	$2.3 \cdot 10^{11}$	$2.7 \cdot 10^{2}$	$7.1 \cdot 10^{15}$
B_0 (T)	$7.8 \cdot 10^{2}$	$8.9 \cdot 10^{-7}$	$2.8 \cdot 10^{7}$

Table 2.1: Scaling factors for the dimensionless E/M problem formulation. Values for Al.

very expensive program. The second problem has to do with the two possible sets of values for ρ_0, J_0, E_0 and B_0. Their existence reflects the disparity between the number of conduction electrons available in a metal and the amount of them that are actually utilized in the transmission of current in our application. The issue is that both ρ and $\dot{\rho}$ appear in our equations (eqns. (2.48) and (2.49)). Picking then either of the scaling factor sets will lead to dimensionless values for ρ that are orders of magnitude larger or smaller than unity in one of the two respective equations.

If we do not make the instant electron current response assumption, eq. (2.44) is replaced by:

$$\frac{\partial \vec{J}}{\partial t} = \frac{q_e}{m_e}\frac{t_0}{J_0}\left(\rho_0 E_0 \rho \vec{E} + J_0 B_0 \vec{J} \times \vec{B} - \rho_0 \tau_0 J_0 \rho \tau \vec{J}\right) \tag{2.50}$$

which in turn replaces the last two conditions in eqns. (2.45). The new set of conditions is:

$$\left.\begin{aligned} \tfrac{t_0 c^2 B_0}{L_0 E_0} &= 1 \\ \tfrac{B_0}{L_0} &= \mu_0 J_0 \\ \tfrac{t_0 E_0}{L_0 B_0} &= 1 \\ \tfrac{t_0 J_0}{L_0 \rho_0} &= 1 \\ \tfrac{t_0}{J_0}\tfrac{q_e}{m_e}\rho_0 E_0 &= 1 \\ \rho_0 E_0 &= J_0 B_0 \\ \rho_0 E_0 &= \rho_0 J_0 \tau_0 \end{aligned}\right\} \Rightarrow \left\{\begin{aligned} \tfrac{t_0 c^2 t_0}{L_0^2} &= 1 \\ L_0 &= \tfrac{B_0}{\mu_0 J_0} \\ B_0 &= \tfrac{t_0}{L_0} E_0 \\ \tfrac{\rho_0 E_0 t_0}{B_0 L_0 \rho_0} &= 1 \\ \rho_0 &= \tfrac{J_0 m_e}{t_0 E_0 q_e} \\ J_0 &= \tfrac{\rho_0 E_0}{B_0} \\ E_0 &= J_0 \tau_0 \end{aligned}\right\} \Rightarrow \left\{\begin{aligned} t_0 &= \tfrac{\tau_0}{c^2 \mu_0} \\ L_0 &= \tfrac{\tau_0}{c \mu_0} \\ t_0 &= \tfrac{L_0}{c} \\ J_0 &= \rho_0 c \\ E_0 &= \rho_0 c \tau_0 \\ B_0 &= \rho_0 \tau_0 \\ \rho_0 &= \tfrac{m_e c^2 \mu_0}{q_e \tau_0^2} \end{aligned}\right. \tag{2.51}$$

The important difference here is, that we have one more independent condition, which allows us to take only one of τ_0 and ρ_0 as a free parameter. Here we've picked the former. With this choice and the previous value for the resistivity of aluminum, we arrive at the values in the third column of table (2.1). The dimensionless form of eq. (2.50) is:

$$\dot{J}_\alpha = \rho E_\alpha + \epsilon_{\alpha\beta\gamma} J_\beta B_\gamma - \rho\tau J_\alpha \tag{2.52}$$

2.3.3.2 Algorithm

We started experimenting with Lax' scheme[24] to numerically integrate eqns. (2.46), (2.47) and (2.48). The spatial averaging required in this algorithm though leads to unrealistic results. For example, in eq. (2.48), averaging causes charge dissipation at the edges of a material, which propagates into the volume, and artificially lowers (or even nulls) the amount of electronic charge (cf. section 2.3.4.2).

Yee's scheme [31], [27] provides a much better alternative for solving eqns. (2.25) and (2.26). In this scheme, the components of the electric and magnetic field in a cell are not centered with respect to the latter. Rather, they are distributed

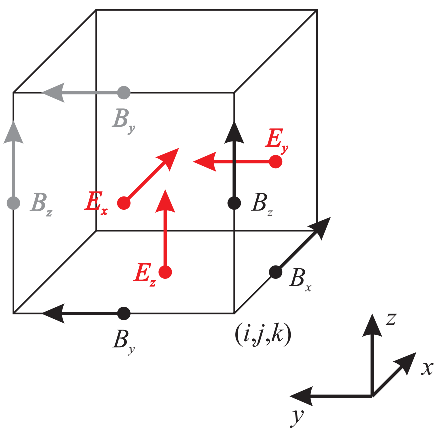

Figure 2.2: Field components in a Yee scheme computational cell

along the edges and faces of the cell in accordance with Ampere's and Faraday's laws (eqns. (2.25) and (2.26) respectively.) The resulting configuration is illustrated in Figure 2.2, where one can see for instance that the x component of $\vec{E}$ is surrounded by the y and z components of $\vec{B}$, tangential to the edges of the face onto which the former is calculated. As far as the integration order is concerned, the algorithm is a leapfrog algorithm, where magnetic and electric fields are updated in alternating half time steps, so that:

$$\vec{E}(t) = f\left(\vec{E}(t - t_{step}), \vec{J}(t - t_{step}), \vec{B}\left(t - \frac{t_{step}}{2}\right)\right) \tag{2.53}$$

and

$$\vec{B}\left(t + \frac{t_{step}}{2}\right) = g\left(\vec{E}(t), \vec{B}\left(t - \frac{t_{step}}{2}\right)\right) \tag{2.54}$$

The current density components entering eq. (2.53), follow the spatial placement of the respective electric field components. They are calculated at the same time points, but at the center of each cell, before they are averaged on its faces. As mentioned before, they are the solutions of eq. (2.49):

$$\epsilon_{ijk} J_j B_k - \gamma J_i = \rho E_i \Rightarrow$$

$$\begin{pmatrix} -\gamma & B_z & -B_y \\ -B_z & -\gamma & B_x \\ B_y & -B_x & -\gamma \end{pmatrix} \begin{pmatrix} J_x \\ J_y \\ J_z \end{pmatrix} = -\rho \begin{pmatrix} E_x \\ E_y \\ E_z \end{pmatrix}$$

so that:

$$J_\alpha = -\rho \frac{D_\alpha}{D}$$

where:

$$D = \begin{vmatrix} -\gamma & B_z & -B_y \\ -B_z & -\gamma & B_x \\ B_y & -B_x & -\gamma \end{vmatrix} \Rightarrow$$

$$D = -\gamma \begin{vmatrix} -\gamma & B_x \\ -B_x & -\gamma \end{vmatrix} - B_z \begin{vmatrix} -B_z & B_x \\ B_y & -\gamma \end{vmatrix} - B_y \begin{vmatrix} -B_z & -\gamma \\ B_y & -B_x \end{vmatrix} \Rightarrow$$

$$D = -\gamma(\gamma^2 + B_x^2) - B_z(\gamma B_z - B_x B_y) - B_y(B_z B_x + \gamma B_y) \Rightarrow$$

$$D = -\gamma^3 - \gamma B_x^2 - \gamma B_z^2 + B_x B_y B_z - B_x B_y B_z - \gamma B_y^2 \Rightarrow$$

$$D = -\gamma(\gamma^2 + B_x^2 + B_y^2 + B_z^2)$$

while:

$$D_x = \begin{vmatrix} E_x & B_z & -B_y \\ E_y & -\gamma & B_x \\ E_z & -B_x & -\gamma \end{vmatrix} \Rightarrow$$

$$D_x = E_x \begin{vmatrix} -\gamma & B_x \\ -B_x & -\gamma \end{vmatrix} - E_y \begin{vmatrix} B_z & -B_y \\ -B_x & -\gamma \end{vmatrix} + E_z \begin{vmatrix} B_z & -B_y \\ -\gamma & B_x \end{vmatrix} \Rightarrow$$

$$D_x = E_x(\gamma^2 + B_x^2) + E_y(\gamma B_z + B_x B_y) - E_z(\gamma B_y - B_z B_x)$$

$$D_y = \begin{vmatrix} -\gamma & E_x & -B_y \\ -B_z & E_y & B_x \\ B_y & E_z & -\gamma \end{vmatrix} \Rightarrow$$

$$D_y = -E_x \begin{vmatrix} -B_z & B_x \\ B_y & -\gamma \end{vmatrix} + E_y \begin{vmatrix} -\gamma & -B_y \\ B_y & -\gamma \end{vmatrix} - E_z \begin{vmatrix} -\gamma & -B_y \\ -B_z & B_x \end{vmatrix} \Rightarrow$$

$$D_y = E_y(\gamma^2 + B_y^2) + E_z(\gamma B_x + B_y B_z) - E_x(\gamma B_z - B_x B_y)$$

$$D_z = \begin{vmatrix} -\gamma & B_z & E_x \\ -B_z & -\gamma & E_y \\ B_y & -B_x & E_z \end{vmatrix} \Rightarrow$$

$$D_z = E_x \begin{vmatrix} -B_z & -\gamma \\ B_y & -B_x \end{vmatrix} - E_y \begin{vmatrix} -\gamma & B_z \\ B_y & -B_x \end{vmatrix} + E_z \begin{vmatrix} -\gamma & B_z \\ -B_z & -\gamma \end{vmatrix} \Rightarrow$$

$$D_z = E_z(\gamma^2 + B_z^2) + E_x(\gamma B_y + B_z B_x) - E_y(\gamma B_x - B_y B_z)$$

where $\vec{E}$ and $\vec{B}$ have been spatially averaged to the center of each cell for these calculations.

As far as the charge density is concerned, the numerically unstable forward time, centered space (FTCS) algorithm [24] provides a starting point for experimentation with eq. (2.48). This is because the inherent numerical instability of the FTCS algorithm affects only ρ and not the other fields.

2.3.3.3 Applications and Boundary Conditions

We applied this solution to a toy problem, that of a charging capacitor. The boundary conditions were periodic in the x and y directions, corresponding to infinitely repeating systems in the (x, y) plane. In the z direction, we imposed Dirichlet conditions on charge density, $\rho = 0$, at the top and bottom of the system, corresponding to an infinite pool of charge. We imposed Neumann conditions on all the other fields $\left(\frac{\partial \vec{E}}{\partial z} = \frac{\partial \vec{J}}{\partial z} = \frac{\partial \vec{B}}{\partial z} = 0\right)$ there. The charging was driven by an imposed current density at the top and bottom. What we were trying to describe was a capacitor connected to a current source. We faced problems, mainly with oscillatory modes that were hard to damp (see Figure 2.3, for a charge density plot illustrating such oscillations across a section through the center of our system and normal to the capacitor plates).

2.3.3.4 Conclusions

This round of experimentation towards a full Maxwell solver was a useful exercise, but did indicate problems that needed a different framework to be addressed. The main issue was the dependence on very small time steps, that threatened the feasibility of simulations at a useful scale. At best, we could reduce the computational load by just propagating atoms through short electrodynamic steps and performing atomic potential calculations at more infrequent molecular dynamics steps. A more efficient scheme was needed still. Frustration with numerical instabilities compounded our willingness to re-think our approach.

2.3.4 Numerical Implementation - Current Solution

The new approach to solving the electrodynamics problem was the product of the simple realization that, in terms of the mechanical properties of the system, it is only

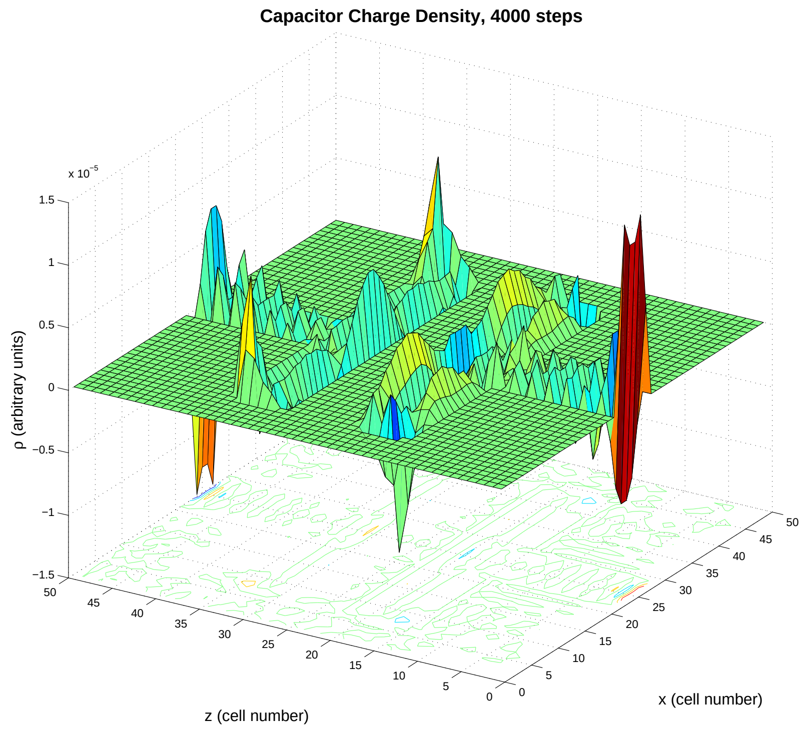

Figure 2.3: Yee method toy problem: Charge density through a section of a capacitor after 4000 numerical steps.

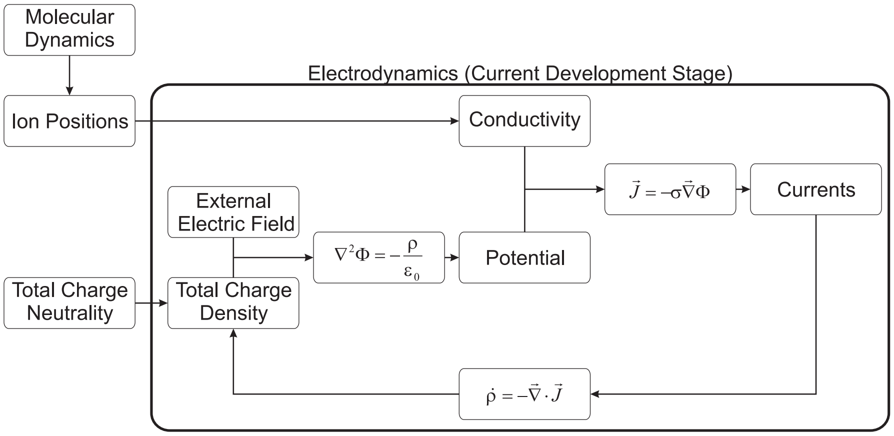

Figure 2.4: Electrodynamic loop

the behavior of atoms that is pertinent. The electrodynamics need only produce the fields that are likely to have an impact on atomic motion. The immediate effect of such a requirement is an effective frequency cutoff (of the order of the inverse MD time step), beyond which fields vary too fast for ions to follow. We therefore decided to consider the atomic configuration produced by each MD step as a frozen background, and calculate the equilibrium $\vec{E}$, $\vec{B}$, $\vec{J}_e$ and ρ_e corresponding to it and our boundary conditions. The hypothesis here was that the electrons, being three orders of magnitude lighter than atoms, will allow the electrodynamic solver to converge fast and allow us to circumvent further ED steps and proceed to the next MD step.

Anxious to put this idea to test we reduced the complexity of the problem, by dropping the magnetic field from our calculations. The equations remaining from our original line-up are then:

$$\nabla^2\Phi = -\frac{\rho}{\epsilon_0} \tag{2.55}$$

$$\frac{\partial\rho_e}{\partial t} = -\vec{\nabla}\cdot\vec{J}_e \tag{2.56}$$

and:

$$\vec{J_e} = -\sigma\vec{\nabla}\Phi \tag{2.57}$$

where we have used the definition:

$$\vec{E} = -\vec{\nabla}\Phi \tag{2.58}$$

Equation (2.57), the modification of eq. (2.37), can be instantly recognized as Ohm's law. Schematically, our current electrodynamic solution is illustrated in Figure 2.4.

2.3.4.1 Poisson Equation

We will use the Fourier transform method to solve the Poisson equation (eq. (2.55)), since the latter has constant coefficients and the boundaries of our problem are parallel to the axes of our Cartesian coordinate system. Following the treatment in reference [24], we will write the finite difference form of eq. (2.55):

$$\begin{aligned}
-\frac{1}{\epsilon_0}\rho_{j,l,k} &= \frac{\Phi_{j+1,l,k} - 2\Phi_{j,l,k} + \Phi_{j-1,l,k}}{d^2} + \\
&+ \frac{\Phi_{j,l+1,k} - 2\Phi_{j,l,k} + \Phi_{j,l-1,k}}{d^2} + \\
&+ \frac{\Phi_{j,l,k+1} - 2\Phi_{j,l,k} + \Phi_{j,l,k-1}}{d^2}
\end{aligned}$$

or:

$$\begin{aligned}
-\frac{d^2}{\epsilon_0}\rho_{j,l,k} &= \Phi_{j+1,l,k} + \Phi_{j-1,l,k} + \\
&+ \Phi_{j,l+1,k} + \Phi_{j,l-1,k} + \\
&+ \Phi_{j,l,k+1} + \Phi_{j,l,k-1} - \\
&- 6\Phi_{j,l,k}
\end{aligned} \tag{2.59}$$

where $d = d_x = d_y = d_z$, so that:

$$\begin{aligned} x_j &= x_0 + jd \quad , \quad j = 0, 1, \ldots, J \\ y_l &= y_0 + ld \quad , \quad l = 0, 1, \ldots, L \\ z_k &= z_0 + kd \quad , \quad k = 0, 1, \ldots, K \end{aligned}$$

and:

$$\Phi_{j,l,k} = \Phi(x_j, y_l, z_k)$$

We will now substitute the Fourier transform of u and ρ to solve this system of equations. Specifically, we will use cosine transforms in the x and y directions, to impose Neumann boundary conditions in the corresponding boundaries ($\partial\Phi/\partial x = 0$ and $\partial\Phi/\partial y = 0$ respectively). On the other hand, we will use a sine transform in the z direction, so that we can enforce Dirchlet boundary conditions and specify the voltages at the top and bottom of the system. We will write then:

$$\Phi_{j,l,k} = \Phi^B_{j,l,k} + \frac{2^3}{JLK} \sum_{m=0}^{J}{}'' \sum_{n=0}^{L}{}'' \sum_{p=1}^{K-1} \hat{\Phi}_{m,n,p} \cos\left(\frac{\pi j m}{J}\right) \cos\left(\frac{\pi l n}{L}\right) \sin\left(\frac{\pi k p}{K}\right) \tag{2.60}$$

and:

$$\rho_{j,l,k} = \frac{2}{J}\frac{2}{L}\frac{2}{K} \sum_{m=0}^{J}{}'' \sum_{n=0}^{L}{}'' \sum_{p=1}^{K-1} \hat{\rho}_{m,n,p} \cos\left(\frac{\pi j m}{J}\right) \cos\left(\frac{\pi l n}{L}\right) \sin\left(\frac{\pi k p}{K}\right) \tag{2.61}$$

The double primes on the sums indicate that the first and last term in them must be multiplied by 1/2. $\Phi^B_{j,l,k}$ is:

$$\Phi^B_{j,l,k} = \left\{ \begin{array}{cc} +\frac{\Delta V}{2} & k = K \\ 0 & k \in [1, K-1] \\ -\frac{\Delta V}{2} & k = 0 \end{array} \right\},\ j \in [0, J],\ l \in [0, L]$$

ΔV being the prescribed voltage difference between the top and bottom of the simulation volume. When substituted into eq. (2.59), these expansions (eq. (2.60) and (2.61)) yield:

$$2\left(\cos\left(\frac{\pi m}{J}\right) + \cos\left(\frac{\pi n}{L}\right) + \sin\left(\frac{\pi p}{K}\right) - 3\right)\hat{\Phi}_{m,n,p} = -\frac{d^2}{\epsilon_0}\hat{\rho}_{m,n,p} \Rightarrow$$

$$\hat{\Phi}_{m,n,p} = -\frac{d^2}{\epsilon_0}\frac{\hat{\rho}_{m,n,p}}{2\left(\cos\left(\frac{\pi m}{J}\right) + \cos\left(\frac{\pi n}{L}\right) + \cos\left(\frac{\pi p}{K}\right) - 3\right)} \tag{2.62}$$

$\hat{\rho}_{m,n,p}$ can be found for the given charge distribution by the inverse transform:

$$\hat{\rho}_{m,n,p} = {\sum_{j=0}^{J}}'' {\sum_{l=0}^{L}}'' \sum_{k=1}^{K-1} \rho^B_{j,l,k} \cos\left(\frac{\pi j m}{J}\right)\cos\left(\frac{\pi l n}{L}\right)\sin\left(\frac{\pi k p}{K}\right) \tag{2.63}$$

where:

$$\rho^B_{j,l,k} = \left\{ \begin{array}{cc} \rho_{j,l,k} & k \in [2, K-2] \cap \{0, K\} \\ \rho_{j,l,1} - \frac{\epsilon_0}{d^2}\frac{\Delta V}{2} & k = 1 \\ \rho_{j,l,K-1} + \frac{\epsilon_0}{d^2}\frac{\Delta V}{2} & k = K-1 \end{array} \right. \tag{2.64}$$

To simplify the implementation of this solver, we will use the operators:

$$\mathcal{S}^p_q\{f(q)\} = \sum_{q=1}^{Q-1} f(q)\sin\left(\frac{\pi p q}{Q}\right) \tag{2.65}$$

and:

$$\mathcal{C}_q^p\{f(q)\} = \sum_{q=0}^{Q}{}'' f(q)\cos\left(\frac{\pi pq}{Q}\right) \tag{2.66}$$

to write eqns. (2.63) and (2.60) as successive one-dimensional transforms:

$$\hat{\rho}_{m,n,p} = \mathcal{C}_j^m\{\mathcal{C}_l^n\{\mathcal{S}_k^p\{\rho_{j,l,k}^B\}\}\} \tag{2.67}$$

and:

$$\Phi_{j,l,k} = \frac{2}{J}\frac{2}{L}\frac{2}{K}\mathcal{C}_m^j\{\mathcal{C}_n^l\{\mathcal{S}_p^k\{\hat{\Phi}_{m,n,p}\}\}\} \tag{2.68}$$

respectively.

The Poisson equation solver is one of the most complicated components of the present version of the electrodynamics solver. In our implementation, we have utilized the optimized, parallelized, FFTW library[12], to perform the necessary fast Fourier transforms. The Poisson solver was checked and debugged thoroughly with test systems. For instance, in Figure 2.5, results for the potential along the plane passing through the centers of two oppositely charged spherical shells are shown.

2.3.4.2 Charge Continuity Equation

According to Numerical Recipes [24], the charge continuity equation (eq. (2.56)) is ideally suited to numerical integration through the Lax algorithm. This was therefore our first choice in calculating the evolution of charge density through our system. Under Lax, the theoretical instability of the finite difference form:

$$\begin{aligned} -\frac{\rho_{e\{j,l,k\}}^{n+1} - \rho_{e\{j,l,k\}}^{n}}{\Delta t} &= \frac{J_{e,x\{j+1,l,k\}}^{n} - J_{e,x\{j-1,l,k\}}^{n}}{2d} + \\ &+ \frac{J_{e,y\{j,l+1,k\}}^{n} - J_{e,y\{j,l-1,k\}}^{n}}{2d} + \end{aligned} \tag{2.69}$$

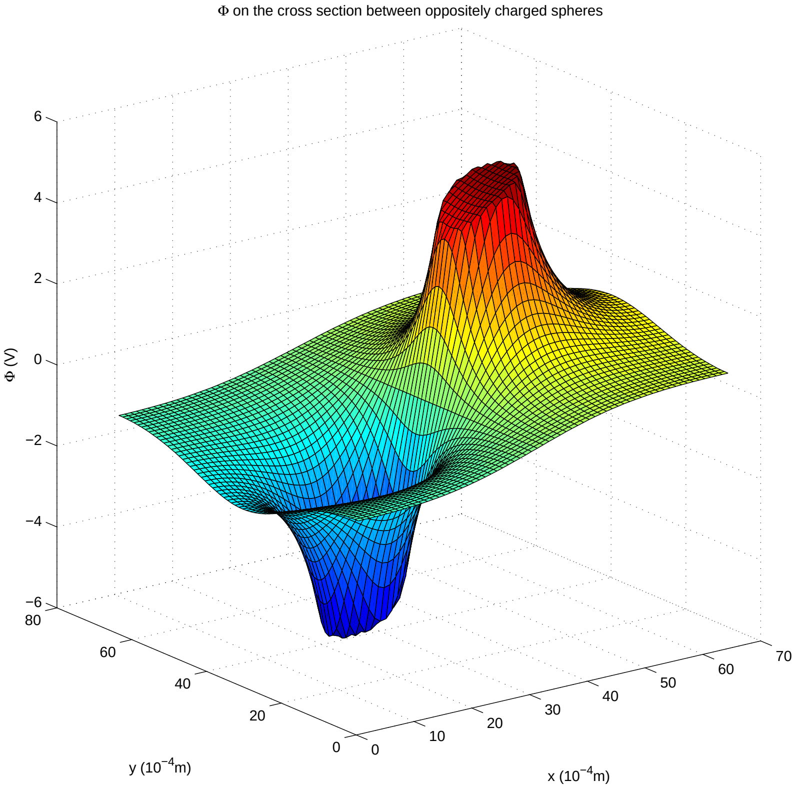

Figure 2.5: Potential along the plane passing through the centers of two oppositely charged spherical cells

$$+ \quad \frac{J^n_{e,z\{j,l,k+1\}} - J^n_{e,z\{j,l,k-1\}}}{2d}$$

corresponding to the Forward Time Centered Space (FTCS) algorithm, can be cured by substituting $\rho^n_{e\{j,l,k\}}$ with an average over its neighboring cells:

$$\rho^n_{e\{j,l,k\}} \approx \frac{\rho^n_{e\{j+1,l,k\}} + \rho^n_{e\{j-1,l,k\}} + \rho^n_{e\{j,l+1,k\}} + \rho^n_{e\{j,l-1,k\}} + \rho^n_{e\{j,l,k+1\}} + \rho^n_{e\{j,l,k-1\}}}{6}$$

We then have:

$$\begin{aligned}
\rho^{n+1}_{e\{j,l,k\}} &= \frac{1}{6}(\rho^n_{e\{j+1,l,k\}} + \rho^n_{e\{j,l+1,k\}} + \rho^n_{e\{j,l,k+1\}} + \\
&+ \rho^n_{e\{j-1,l,k\}} + \rho^n_{e\{j,l-1,k\}} + \rho^n_{e\{j,l,k-1\}}) - \\
&- \frac{\Delta t}{2d}[J^n_{e,x\{j+1,l,k\}} + J^n_{e,y\{j,l+1,k\}} + J^n_{e,z\{j,l,k+1\}} - \\
&- J^n_{e,x\{j-1,l,k\}} - J^n_{e,y\{j,l-1,k\}} - J^n_{e,z\{j,l,k-1\}}] \qquad (2.70)
\end{aligned}$$

where the upper indexes refer to the time-step, corresponding to the value of the quantity, so that:

$$t^n = t^0 + n\Delta t$$

The problem with applying this algorithm to our system appears at the exposed surfaces of the conducting materials. There, the averaging over the neighboring cells, that is imposed by the Lax scheme, leads to loss of charge density into non-conducting volume. We therefore have to check and exclude the charge density contributions of such cells, corresponding to non-conducting volumes, to the averages. On the same theme, we do not calculate eq. (2.70) onto such non-conducting cells either.

The added complications led us to check the performance of the basic FTCS scheme. Given that charge density is reset to zero at each MD time step, that a very small number of ED steps are required to achieve an equilibrium state and that the charge imbalances in a conductor should be limited, we expected that there should not be instability problems. Indeed, theoretical analysis (cf. section 2.3.4.6), as well as our tests, justified our optimism and FTCS has become our default integration algorithm for eq. (2.56).

2.3.4.3 Ohm's Law

To calculate the electron current induced by the potential Φ we use Ohm's law (eq. (2.57)). We write this equation in finite difference form, employing a second-order representation for the spatial derivatives:

$$J_{e,x\{j,l,k\}} = -\sigma_{j,l,k} \frac{\Phi_{j+1,l,k} - \Phi_{j-1,l,k}}{2d} \tag{2.71}$$

and similarly for the other two dimensions. One should note here that, since we consider our atoms fixed between MD steps, the conductivity in our system is dependent only on position and not time, during each cycle of ED steps.

2.3.4.4 Dimensionless Form

Once again, we had to make sure that our equations don't explore the limits of machine precision. This time though, it was their discretization that informed our scaling choices. We therefore picked a unit system where:

$$\Delta\tilde{t} = \tilde{d} = \tilde{e} = \tilde{\epsilon}_0 = 1$$

In this system, equations (2.59), (2.69) and (2.71) become:

$$\begin{aligned} -\tilde{\rho}_{j,l,k} &= \tilde{\Phi}_{j+1,l,k} + \tilde{\Phi}_{j-1,l,k} + \\ &+ \tilde{\Phi}_{j,l+1,k} + \tilde{\Phi}_{j,l-1,k} + \\ &+ \tilde{\Phi}_{j,l,k+1} + \tilde{\Phi}_{j,l,k-1} - \\ &- 6\tilde{\Phi}_{j,l,k} \end{aligned} \tag{2.72}$$

$$\begin{aligned} -\left(\tilde{\rho}^{n+1}_{e\{j,l,k\}} - \tilde{\rho}^{n}_{e\{j,l,k\}}\right) &= \frac{\tilde{J}^n_{e,x\{j+1,l,k\}} - \tilde{J}^n_{e,x\{j-1,l,k\}}}{2} + \\ &+ \frac{\tilde{J}^n_{e,y\{j,l+1,k\}} - \tilde{J}^n_{e,y\{j,l-1,k\}}}{2} + \\ &+ \frac{\tilde{J}^n_{e,z\{j,l,k+1\}} - \tilde{J}^n_{e,z\{j,l,k-1\}}}{2} \end{aligned} \tag{2.73}$$

and:

$$\tilde{J}_{e,x\{j,l,k\}} = -\tilde{\sigma}_{j,l,k} \frac{\tilde{\Phi}_{j+1,l,k} - \tilde{\Phi}_{j-1,l,k}}{2} \tag{2.74}$$

respectively, where:

$$\rho = \frac{e}{d^3}\tilde{\rho}$$

$$J_{e,\alpha} = \frac{e}{d^2 \Delta t}\tilde{J}_{e,\alpha}$$

$$\Phi = \frac{e}{\epsilon_0 d}\tilde{\Phi}$$

and:

$$\sigma = \frac{\epsilon_0}{\Delta t}\tilde{\sigma}$$

Using cell sizes of order $d \sim 10^{-10}$m, as we will do in our experiments, we will have only a few atoms per cell, therefore at a maximum $\tilde{\rho} \sim 10$, but really much less than that, as we do not expect charge neutrality to be upset by more than a fraction of an electron charge, given the shielding effect due to the free electrons. Furthermore, for Al and Cu, with conductivities of $3.77 \cdot 10^7$S/m and $5.96 \cdot 10^7$S/m respectively, and using a time step of order $\Delta t \sim 10^{-19}$s per Table (2.1), we get $\tilde{\sigma}_{Al} = 0.426$ and $\tilde{\sigma}_{Cu} = 0.673$. We will anticipate later discussion of the thermal limits to the voltage applied across our system (cf. section 3.1.4) and provide an estimate of $\Delta V \sim 10^{-2}$V for it, which yields $\Delta\tilde{V} \sim 6 \cdot 10^{-5}$, which in turn suggests a maximum current density value of $\tilde{J} \sim 4 \cdot 10^{-5}$. We have managed then, in this system of units, to both simplify our equations and to compact the values of the terms involved closer to unity, avoiding the extremes of machine precision.

2.3.4.5 Boundary Conditions

The boundary conditions for the chosen implementation describe a system that is located between two electrically connected, infinitely conducting plates, at a prescribed voltage difference ΔV, at its two z-axis extremes. In terms of the specific equations, $+\Delta V/2$ and $-\Delta V/2$ are the boundary values of Φ at z_{max} and z_{min} respectively for the Poisson equation, while the total charge density:

$$\rho_{tot} = \rho_i + \rho_e$$

is always taken to be zero at these points ($\rho_e = -\rho_i$) creating two pools of charge for the charge continuity equation.

We assume the xz and yz sides of the system to be removed enough from active regions for zero gradient conditions to be appropriate there for the Poisson equation.

Ohm's law is handled at the boundaries, not through conditions, but by halving the stepping for the affected differences, which are now taken between the boundary cell and its first neighbor in the direction normal to the boundary. The same treatment is applied to the charge continuity equation at the xz and yz sides only.

2.3.4.6 Von Neumann Stability Analysis

The stability of our system of finite-difference equations can be explored through the von Neumann stability analysis. Specifically, we will find the temporal growth rates for the eigenmodes of Φ in our system and show them to be in the interval (0,1] for realistic parameters. To that end, we will make a Fourier expansion of the quantity of interest:

$$\begin{aligned}
\Phi^n_{\{j,l,k\}} &= \sum_{\omega} \sum_{\kappa_x,\kappa_y,\kappa_z} \phi^{\omega}_{\{\kappa_x,\kappa_y,\kappa_z\}}(n,j,l,k) \Leftrightarrow \\
\Phi^n_{\{j,l,k\}} &= \sum_{\omega} \sum_{\kappa_x,\kappa_y,\kappa_z} B_{\omega,\kappa_x,\kappa_y,\kappa_z} e^{i\omega n \Delta t} e^{id(\kappa_x j+\kappa_y l+\kappa_z k)}
\end{aligned}$$

We note that our system is linear in time. For the purposes of this analysis, we will also assume that the conductivity is uniform, in which case the linearity is carried over to the spatial dimensions as well. We will work with the dimensionless form of our system but for the sake of simplicity we will not carry the tilde. Using eq. (2.74) we can write eq. (2.73) as:

$$\begin{aligned}
\rho^{n+1}_{i\{j,l,k\}} + \rho^{n+1}_{e\{j,l,k\}} - \rho^{n}_{i\{j,l,k\}} - \rho^{n}_{e\{j,l,k\}} = -& \frac{\sigma}{4}\Big(\Phi^n_{\{j+2,l,k\}} + \Phi^n_{\{j-2,l,k\}} + \\
+& \Phi^n_{\{j,l+2,k\}} + \Phi^n_{\{j,l-2,k\}} + \\
+& \Phi^n_{\{j,l,k+2\}} + \Phi^n_{\{j,l,k-2\}} - \\
-& 6\Phi^n_{\{j,l,k\}}\Big) \Rightarrow
\end{aligned}$$

$$\begin{aligned} \rho^{n+1}_{e\{j,l,k\}} = -& \frac{\sigma}{4}\Big(\Phi^{n}_{\{j+2,l,k\}} + \Phi^{n}_{\{j-2,l,k\}} + \Phi^{n}_{\{j,l+2,k\}} + \Phi^{n}_{\{j,l-2,k\}} + \\ +& \Phi^{n}_{\{j,l,k+2\}} + \Phi^{n}_{\{j,l,k-2\}} - 6\Phi^{n}_{\{j,l,k\}}\Big) + \rho^{n}_{e\{j,l,k\}} \end{aligned} \tag{2.75}$$

Note that, during the stepping of our electrodynamics we consider the ions stationary, so that $\rho^{n+1}_{i\{j,l,k\}} = \rho^{n}_{i\{j,l,k\}}$. Now, with a double application of the Poisson equation (eq. (2.72)):

$$\begin{gathered} \Phi^{n+1}_{j+1,l,k} + \Phi^{n+1}_{j-1,l,k} + \Phi^{n+1}_{j,l+1,k} + \Phi^{n+1}_{j,l-1,k} + \Phi^{n+1}_{j,l,k+1} + \Phi^{n+1}_{j,l,k-1} - 6\Phi^{n+1}_{j,l,k} = \\ = -\tfrac{\sigma}{4}\Big(\Phi^{n}_{\{j+2,l,k\}} + \Phi^{n}_{\{j-2,l,k\}} + \Phi^{n}_{\{j,l+2,k\}} + \Phi^{n}_{\{j,l-2,k\}} + \\ + \Phi^{n}_{\{j,l,k+2\}} + \Phi^{n}_{\{j,l,k-2\}} - 6\Phi^{n}_{\{j,l,k\}}\Big) + \\ + \Phi^{n}_{j+1,l,k} + \Phi^{n}_{j-1,l,k} + \Phi^{n}_{j,l+1,k} + \Phi^{n}_{j,l-1,k} + \Phi^{n}_{j,l,k+1} + \Phi^{n}_{j,l,k-1} - 6\Phi^{n}_{j,l,k} \end{gathered} \tag{2.76}$$

As we mentioned before, this equation is linear in both time and space. It will be therefore valid for each particular mode $\phi^{\omega}_{\{\kappa_x,\kappa_y,\kappa_z\}}$. We note that, by definition:

$$\begin{aligned} \phi^{\omega}_{\{\kappa_x,\kappa_y,\kappa_z\}}(n+1,j,l,k) &= e^{i\omega\Delta t}\phi^{\omega}_{\{\kappa_x,\kappa_y,\kappa_z\}}(n,j,l,k) \\ \phi^{\omega}_{\{\kappa_x,\kappa_y,\kappa_z\}}(n,j+1,l,k) &= e^{i\kappa_x d}\phi^{\omega}_{\{\kappa_x,\kappa_y,\kappa_z\}}(n,j,l,k) \\ &\vdots \end{aligned} \tag{2.77}$$

where $d = \Delta t = 1$ in this system and:

$$\xi = e^{i\omega\Delta t}$$

is the growth rate of the mode, since:

$$\phi^{\omega}_{\{\kappa_x,\kappa_y,\kappa_z\}}(n,j,l,k) = \xi^{n}\phi^{\omega}_{\{\kappa_x,\kappa_y,\kappa_z\}}(0,j,l,k)$$

For a solution to be stable, we must show that $|\xi| \leq 1$.

Armed with eqs. (2.77) we can now write eq. (2.76) for a given mode:

$$\begin{gathered}\xi\left(e^{i\kappa_x d}+e^{-i\kappa_x d}+e^{i\kappa_y d}+e^{-i\kappa_y d}+e^{i\kappa_z d}+e^{-i\kappa_z d}-6\right)= \\ =-\frac{\sigma}{4}\left(e^{2i\kappa_x d}+e^{-2i\kappa_x d}+e^{2i\kappa_y d}+e^{-2i\kappa_y d}+e^{2i\kappa_z d}+e^{-2i\kappa_z d}-6\right)+ \\ +e^{i\kappa_x d}+e^{-i\kappa_x d}+e^{i\kappa_y d}+e^{-i\kappa_y d}+e^{i\kappa_z d}+e^{-i\kappa_z d}-6 \Rightarrow\end{gathered}$$

$$\begin{gathered}\xi\left(cos(\kappa_x d)+cos(\kappa_y d)+cos(\kappa_z d)-3\right)= \\ =-\frac{\sigma}{4}\left(cos(2\kappa_x d)+cos(2\kappa_y d)+cos(2\kappa_z d)-3\right)+ \\ +cos(\kappa_x d)+cos(\kappa_y d)+cos(\kappa_z d)-3 \Rightarrow\end{gathered}$$

$$\xi = 1-\frac{\sigma}{4}\frac{cos(2\kappa_x d)+cos(2\kappa_y d)+cos(2\kappa_z d)-3}{cos(\kappa_x d)+cos(\kappa_y d)+cos(\kappa_z d)-3}$$

A 2D version of this equation:

$$\xi = 1-\frac{\sigma}{4}\frac{cos(2\kappa_x d)+cos(2\kappa_y d)-2}{cos(\kappa_x d)+cos(\kappa_y d)-2}$$

is plotted in Figure 2.6 for the first 30 wavelengths in each direction ($\lambda_\alpha = qd, q \in \mathbb{N}^*$) and $\sigma = 1$. It is obvious that there is no sign inversion for the second term. For stability therefore, we need $\xi > -1$. We find that $\xi > 0$ here for a conductivity density higher than that of either copper or aluminium. Our scheme then satisfies the von Neumann stability analysis criterion.

2.4 Meshing Things Together

Important as the atomic potential and the algorithm for the calculation of electric fields are, they are only fine ingredients for a meal. The pot where the two are to be combined is provided in our case by the open source Hordes Of Little Atoms

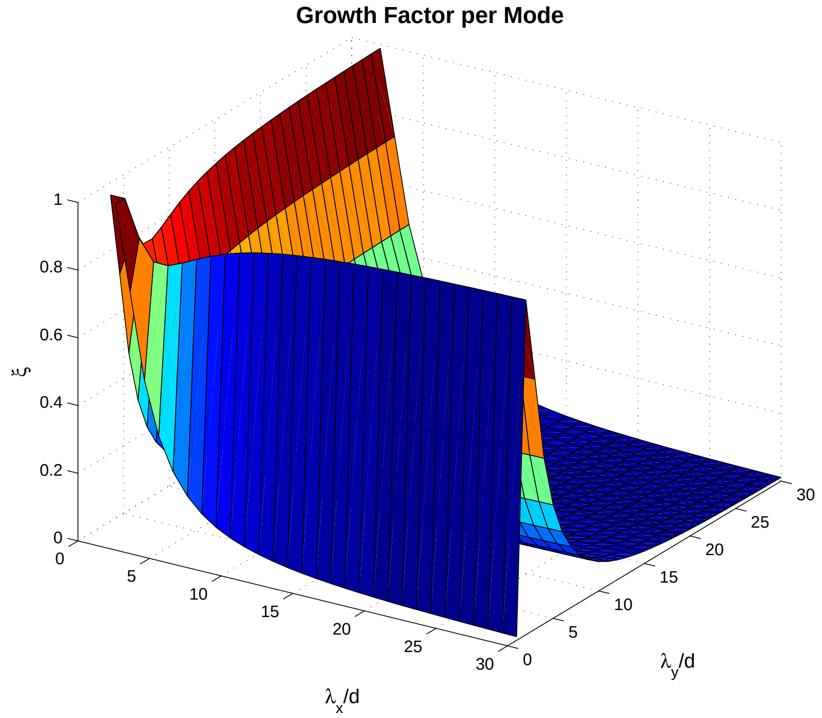

Figure 2.6: von Neumann analysis mode growth, for $\sigma = 1$.

(HOLA) Molecular Dynamics (MD) code. The brain child of Professor Michael Marder, remains in active development and use, for the diverse projects of his group. Over the past years, it has been employed in studies of cracks, shock waves, green leaf and graphene buckling and rubber rupture. The dissertations of Dominic Holland[13] and Matthew Lane[16] present good overviews of the code, its functionality and its interface, at least to the extent that an evolving program exceeding 40,000 lines allows.

The combined MEAM-Rose potential falls easily within the framework of the code. Indeed, HOLA was created from the beginning to allow modularity of the employed potentials. The previous, single species implementation of MEAM provided the skeleton for the updated potential. Still, changes in data structures and parameter input mechanisms were required outside the potential module, to accommodate it.

The electrodynamics module was a novel addition to the HOLA code. In functional terms, the input to the solver comprises of the ion positions at the beginning of each MD step. These are translated into a 3D conductivity distribution. Based on that, the electrodynamics solver finds the equilibrium solution for the electric field throughout the volume of our simulation and the attendant current density. Feedback to the molecular dynamics code is through updates of the velocities of and the forces exerted on the particles. The module translates the electric field data into force contributions for the ions i in each electrodynamic cell (u, v, w):

$$\Delta\vec{F}_i = q_i\vec{E}_{uvw}$$

Furthermore, the current density is translated into ohmic heating per ion in each

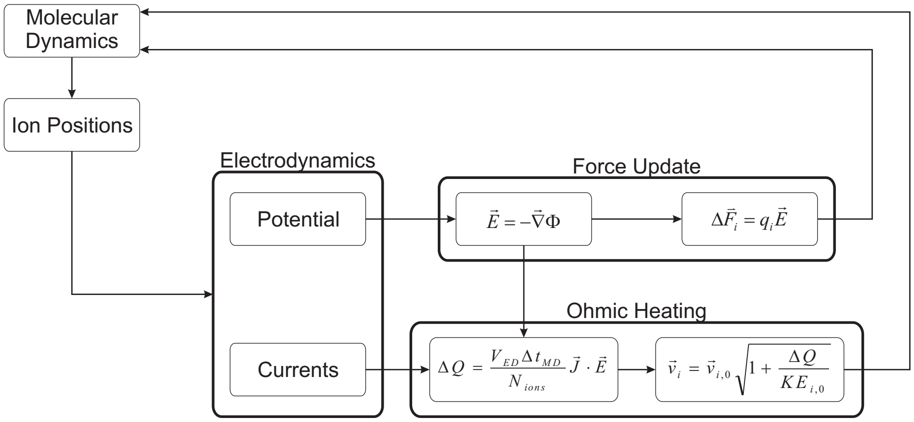

Figure 2.7: MD and ED integration

cell:

$$\Delta Q_{uvw} = \frac{V_{ED}\Delta t_{MD}}{N_{uvw}}\vec{J}_{uvw}\cdot\vec{E}_{uvw}$$

where Δt_{MD} is the MD time step, while V_{ED}, N_{uvw}, $\vec{J}_{uvw}$ and $\vec{E}_{uvw}$ are the volume, number of ions, current density and electric field for the cell. ΔQ_{uvw} is then used to scale the ion velocities:

$$\vec{v}_i = \vec{v}_{i,0}\sqrt{1+\frac{\Delta Q_{uvw}}{\frac{1}{2}m_i v_{i,0}^2}}$$

It should be noted here that the last equation is valid, even if more than one species occupy the cell, according to the equipartition theorem. The process is schematically represented in Figure 2.7.

2.5 Sliding and Sizing

With the basic physics set in code, the remaining task was to set up the simulation of a sliding experiment and the mechanism to measure the forces that determine the coefficient of friction.

To simulate a sliding experiment, we have to create a system comprising of a stylus on a block and produce relative motion. The stylus and the block are created by filling the simulation volume with monocrystals of the respective materials, and then carving out the required objects. The stylus comprises of a hemisphere at the bottom of a vertical circular prism of the same diameter. The block occupies the full lateral extent of the lower part of the computational volume. The HOLA code does not allow parallel processing in more than one direction. We reserve that direction (x) for the relative motion, which puts a premium in space utilization in the other two directions. For realistic asperity radii of several tens of nanometers therefore, we only simulate a tip centered slab of the asperity. The two objects can be prepared at any relative position, as long as there is separation. Penetration can be achieved dynamically, which would also produce the relevant work hardening and make the simulation more realistic.

To effect the sliding, we fix the block and move the stylus. We fix the block by freezing its lower portion, and, optionally, its sides. To freeze a region in the simulation, means to exclude the atoms it encloses from position and velocity updates. These atoms are still taken into account for force calculations. To move the stylus, we also exclude its top from molecular dynamics updates to position and velocity. Instead, we move the respective atoms rigidly, at a constant velocity in the x direction, parallel to the free surface of the block. Along the loading axis (z direction) we try to achieve and maintain a constant force. To do that, we displace the top of the stylus according to the following equation:

$$\Delta z = \begin{cases} -\Delta z_{max} \quad , & \psi < -1 \\ \psi \Delta z_{max} \quad , & -1 \leq \psi \leq 1 \\ +\Delta z_{max} \quad , & 1 < \psi \end{cases}$$

where $\Delta z_{max} > 0$, while:

$$\psi = \frac{P_{target} - P}{P_{target}}$$

with

$$\vec{P}_{target} = -P_{target}\hat{e}_z$$

and

$$\vec{P} = -P\hat{e}_z$$

the target and actual loading force respectively. Effectively then, we limit the speed of vertical motion to:

$$|v_z| \leq \frac{\Delta z_{max}}{\Delta t_{MD}}$$

We do that to avoid creating shocks in the material and therefore keep that speed well bellow the sound speed in the stylus.

To calculate the coefficient of friction, we need to be able to measure the loading ($\vec{P} = -P\hat{e}_z$) and tangential force ($\vec{S} = S\hat{e}_x$) driving the motion. Since the top of the stylus moves at a constant horizontal velocity and is nearly stationary in the z direction, we can apply Newton's action-reaction law to that problem. We will therefore write:

$$P = \sum_i f_{i,z}$$

and

$$S = -\sum_i f_{i,x}$$

where the sums are over the particles of the rigidly moved top of the stylus. Since these forces are subject to fluctuations, we average our measurements over a period that would allow disturbances to be distributed across the slider. A good gauge for that is the sound speed of the material. We currently average at no less than the time of three traversals of half the height of our computational volume by a typical sound wave. The coefficient of friction then is:

$$\mu = -\frac{P}{S}$$

While it is true that we do not control the tangential force $\vec{S}$ and that the top of the slider can be either in motion or moving at a constant speed, we can measure the static coefficient of friction. Starting from a standstill, with the surfaces in contact, we can start the motion of the stylus top at a very low speed and utilize its elasticity, to capture the maximum value of the friction coefficient. That would be its static value, as it would correspond to the moment just before motion commences.

Chapter 3

Simulations

3.1 Putting Things in Perspective

Before any numerical simulation, one needs to establish the parameter space of interest and the range of values that is to be explored for each parameter. In our case, the relevant parameters are the spatial dimensions of the system, the loading force on the contact, its sliding velocity and the voltage applied across the volume. We currently limit ourselves to aluminum and copper as the possible materials for the stylus and the block. The considerations that determine the range of values to be explored vary from practical to physical and we will study them in the following sections.

3.1.1 Spatial Dimensions

To set the spatial dimensions of the system, we need to strike a compromise between physical relevance and computational feasibility.

In terms of physical relevance, we know that typical asperity sizes for polished metals are in the hundreds of Angstroms range. While these may be irregular protrusions, they set a spatial scale and lead us to a minimum slider radius of a few nanometers. Another reason for this minimum is the range of atomic potentials. The latter is in the range of several Angstroms. If we do want to simulate an asperity with a realistic, load bearing tip, parts of it have to be beyond the effective potential range of the opposite surface. It should be noted here, that our reference to a physically relevant size minimum should not discount small scale simulations. According to Bowden and Tabor[8], asperities of that size seem to survive no matter the preparation of the metal surface due to work hardening. As a consequence of their durability, they do represent the contact points between objects.

If physical relevance establishes size minimums, computational feasibility sets corresponding maximums. Hard limits are determined by memory considerations. Softer limits relate to execution times. With respect to memory utilization, it is hard to quantify the overhead due to each individual subroutine of the code, especially given the transient nature of local variables. However, we know the variables per particle that are stored in allocated space, and the size of most of them, which should give us a good first estimate of the capacity of our system.

HOLA utilizes the Verlet algorithm[28, 29, 20], which requires the current positions of the particles, the forces acting on them, and the previous step positions, to produce the particle positions for the next step. In addition, we store the momentum, potential and kinetic energy per particle, to speed up calculations. These are 14 double precision real (64 bit) variables. Each particle carries a type designation and three coordinates corresponding to a compartmentalization of the simulation volume, that aids neighbor finding. The number of those neighbors and the first relevant entry in a big list also accompany each particle. These are 6 integer (32 bit) variables. The MEAM subroutine also keeps a neighbor list for the unscreened interactions of each particle, requiring again 2 integer (32 bit) variables per particle to navigate. It also keeps a list of screening factors for each neighbor pair and the distance of the most remote unscreened neighbor per particle. The latter adds another double precision real (64 bit) variable per particle. Of the three lists mentioned, the two neighbor lists have elements of integer (32 bit) type and the screening factors list has elements of double precision real (64 bit) type. The size of these is the number of particles times the anticipated maximum number of neighbors, usually set to 100 per atom. The grand total per atom in this calculation is 14016 bits or 1752 bytes. Depending on the definition of a gigabyte (1024^3 or 10^9 bytes) this number allows data for approximately $6 \cdot 10^5$ particles per gigabyte (GB) to be stored. Auxiliary allocated space and local variables, as well as system overhead, bring this number down, but a good order of magnitude estimate is established. Our current production machine, Lonestar, at the Texas Advanced Computing Center (TACC), makes approximately 2GB available per processor, so systems of order 10^5 particles per processor should be feasible. For copper, the denser of the two metals we currently study, the equilibrium density is 84.3atoms/nm^3, given a side of 3.62Å per fcc cell. Therefore, a volume of order 10^3nm^3 should fit in each processor.

Another limit is imposed by computation time per atom per processor. These computations are performed serially in each processor. There is therefore another benefit to spread our system across multiple processors. Beyond the memory limitations, this addresses the issue of parallelizing computations. The issue here is the availability of processors and the costs of communication between them, every time information needs to be exchanged. The latter is exchanged over paths that are typically orders of magnitude slower than the memory bus between the processor and its local memory. One needs to strike a compromise between maximizing work parallelization and minimizing inter-processor communications. Rigorous analysis here is more involved, and we took an empirical approach, of running tests and settling on a good balance for our simulation.

3.1.2 Loading Force

Previous experiments have shown that, for most applications, the strength of the contact points between surfaces is equal to the local yield strength of the softer material. If more force is applied, the material flows to increase the contact area and keep the pressure constant. If load is removed, the relaxation of elastic deformations in the surrounding area tends to cause surface separation in all but the softer metals. It would appear then, that all we have to do is look up the yield strength of aluminum (the softer of the two metals) and prescribe the corresponding normal force for the contact area we want to create. While this is a good starting point, we have to remember that work hardening and the structure of the specimen (orientation for a single crystal or distribution of crystallites in a polycrystalline piece) will affect its yield strength. We should therefore not expect to achieve the exact calculated contact area with this process.

The measure of yield strength most pertinent to our system is the Brinell hardness. It is found through measurements of the size of indentation, produced by a hard sphere, onto a flat surface of the tested material. For copper and aluminum, these values[1] are 874MPa and 245MPa respectively. The copper value is in agreement with experimental fits reported by Bowden and Tabor.

---

[1] As found on the webelements.com website, quoting: G.V. Samsonov (Ed.) in *Handbook of the physicochemical properties of the elements*, IFI-Plenum, New York, USA, 1968

3.1.3 Relative Velocity

The scale in terms of sliding velocity is set by the sound speeds of the two materials. At and beyond those speeds, shock fronts will be created and propagate in Mach cones within each material. Quoted values[2] for aluminum and copper are 5.1km/s and 3.57km/s respectively. Just as with hardness, these values depend on the history, as well as the structure of the specimen (orientation for a single crystal or distribution of crystallites in a polycrystalline piece). It should be noted, that these speeds are of the same order of magnitude as the intended projectile velocities for a railgun.

Very low speeds are also relevant for friction studies. As mentioned earlier (cf. section 2.5), at very low speeds we can observe the transition from static to kinetic friction and measure the former.

3.1.4 Applied Voltage

The two most direct effects of voltage on our system are creation of magnetic pressure and heat deposition, due to the generated currents. Magnetic forces act primarily on the $x-y$ plane. They are not accounted for in the current electrodynamic solver, although they can create stresses comparable to the tensile strengths of our materials, for high enough values of the electric current density. Heat deposition raises the temperature of the materials, thus affecting their elastic and plastic properties and leading to melting or evaporation. It is the solid to liquid transition that we will utilize to set a scale for the applied voltage.

Let us simplify the problem, consider a uniform, prismatic resistor such as the one in Figure 3.1, and try to find the temperature profile along its axis (x). We will assume that its ends are at contact with heat baths of temperature T_0 and that

---

[2] As found on the webelements.com website, quoting: G.V. Samsonov (Ed.) in *Handbook of the physicochemical properties of the elements*, IFI-Plenum, New York, USA, 1968

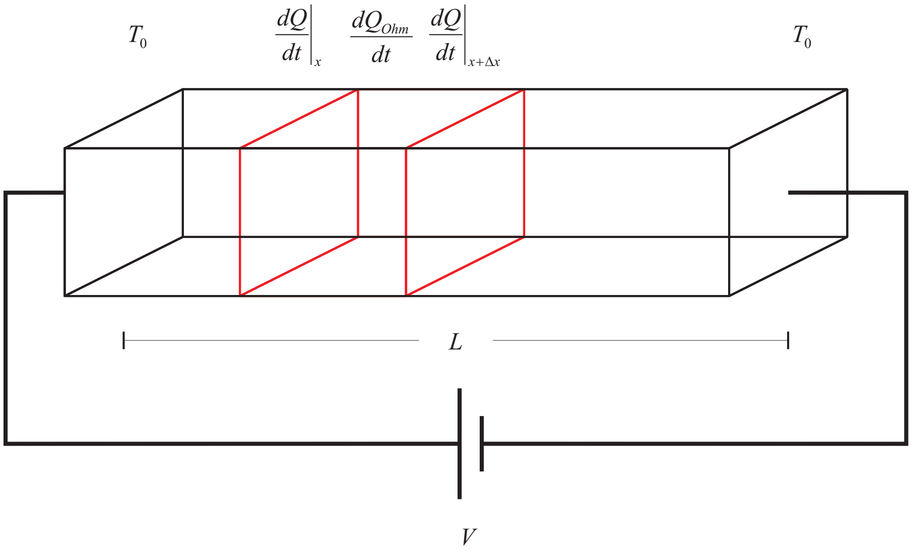

Figure 3.1: Heat flux in prismatic resistor

a voltage V is applied across it. For a slice of this prism between x and $x + \Delta x$, we have three heat contributions. First, there is the ohmic heat generated by the current flowing through it:

$$\frac{dQ_{Ohm}}{dt} = \vec{J} \cdot \vec{E} A \Delta x = \sigma \vec{E}^2 A \Delta x$$

where A is the surface area of the base of the prism. Then, we have the heat flowing into the slice from the left and that leaving from the right:

$$\left.\frac{dQ}{dt}\right|_x = -kA \left.\frac{dT}{dx}\right|_x$$

and

$$\left.\frac{dQ}{dt}\right|_{x+\Delta x} = -kA \left.\frac{dT}{dx}\right|_{x+\Delta x}$$

respectively, where k is the thermal conductivity of the material. When the system is in thermal equilibrium, no net heat should be trapped in the slice, meaning that:

$$\left.\frac{dQ}{dt}\right|_x + \frac{dQ_{Ohm}}{dt} - \left.\frac{dQ}{dt}\right|_{x+\Delta x} = 0 \Rightarrow$$

$$\left.\frac{dQ}{dt}\right|_x + \frac{dQ_{Ohm}}{dt} = \left.\frac{dQ}{dt}\right|_{x+\Delta x}$$

or

$$-k\left.\frac{dT}{dx}\right|_x + \sigma\vec{E}^2\Delta x = -k\left.\frac{dT}{dx}\right|_{x+\Delta x} \Rightarrow$$

$$\sigma\vec{E}^2 = -k\frac{\left.\frac{dT}{dx}\right|_{x+\Delta x} - \left.\frac{dT}{dx}\right|_x}{\Delta x}$$

and, if we take the limit of $\Delta x \to 0$:

$$\sigma\vec{E}^2 = \lim_{\Delta x\to 0}\left(-k\frac{\left.\frac{dT}{dx}\right|_{x+\Delta x} - \left.\frac{dT}{dx}\right|_x}{\Delta x}\right) = -k\frac{d^2T}{dx^2} \Rightarrow$$

$$\frac{d^2T}{dx^2} = -\frac{\sigma}{k}\vec{E}^2$$

which, given eq. (2.58), and because the system is one dimensional, becomes:

$$\frac{d^2T}{dx^2} = -\frac{\sigma}{k}\left(\frac{d\Phi}{dx}\right)^2 = -\frac{\sigma}{kL^2}V^2$$

where L is the length of the whole prism, across which voltage V is applied. We have assumed here that resistance is not affected by temperature, so that the voltage drop is linear along the length of the prism. We need to integrate this equation twice to find the temperature profile along the length of the prism. The first integration yields:

$$\frac{dT}{dx} = -\frac{\sigma V^2}{kL^2}x + C$$

And, from the second integration:

$$T = -\frac{\sigma V^2}{2kL^2}x^2 + Cx + D$$

C and D can be determined by the condition that the edges of the system be at equilibrium with heat baths of temperature T_0:

$$T(x = 0) = D = T_0$$

and:

$$T(x = L) = -\frac{\sigma V^2}{2kL^2}L^2 + CL + T_0 = T_0 \Rightarrow$$

$$C = \frac{\sigma V^2}{2kL}$$

From symmetry, the temperature maximum is at $x = L/2$, where:

$$T_{max} = \frac{\sigma V^2}{8k} + T_0 \tag{3.1}$$

independent of the length or area of the prism. For copper, the electrical and thermal conductivities, as well as the melting point are[1] $\sigma_{Cu}^{900K} = 1.66 \cdot 10^7$S/m, $k_{Cu} = 4.01$W/(cmK) and $T_{mp,Cu} = 1084.62°$C respectively. For aluminum, the same numbers are[1] $\sigma_{Al}^{900K} = 9.82 \cdot 10^6$S/m, $k_{Al} = 2.37$W/(cmK) and $T_{mp,Al} = 660.32°$C respectively. If the heat baths are at $T_0 = 27°$C, solving eq. (3.1) for V and substituting the melting point for T_{max}, we find the maximum voltage that can be applied to the conductor before it melts. The values we find are $V_{max,Cu} = 45.2$mV and $V_{max,Al} = 35$mV. Do note that the electrical conductivity changes significantly with temperature and we took the values listed closer to the melting temperatures, for our calculations.

The values derived above only set a scale for the voltage differences to be applied across our system. The limitations of our calculation are both due to our approximations and the simplifications in our simulation. The shape of our system is more complicated than a uniform prism, but, to first order, it can be considered as two prisms stacked on top of each other, each made from different materials. Such a system of course opens up the issue of spreading resistance at the junction between the two prisms. Furthermore, the effect of thermal expansion was ignored, but the final result is indeed independent of the size of the prism. On the simulation side, an anticipated issue is with the temperature dependence of the electrical resistance, which is not taken into account currently. One way to alleviate this problem is to set the heat baths near the target temperature and use the corresponding electrical conductivities for our physics. This would lower the available range of voltages though, since $\Delta T \propto V^2$, according to eq. (3.1).

3.2 Molecular Dynamics

Our first MD-only production runs have been intended to establish the functionality of the code on the target computational platform. They were extended when interesting results started being produced. Experience with previous simulations led us to choose a time step $\Delta t_{MD} = 0.5 \cdot 10^{-15}$s for the molecular dynamics. In terms of spatial extent, the computational volume dimensions were set at: $L_x = 50.0$nm, $L_y = 6.0$nm, $L_z = 5.0$nm. The stylus was carved from aluminum, with a radius $R = 25.0$nm and it was placed a distance $d = 4.0$Å away from a copper block of height $h = 2.0$nm. The distance between the stylus and the block was chosen so that the interaction between the surfaces is well into the potential tail. Therefore, pressure rises gradually as the stylus is lowered. The starting configuration of the

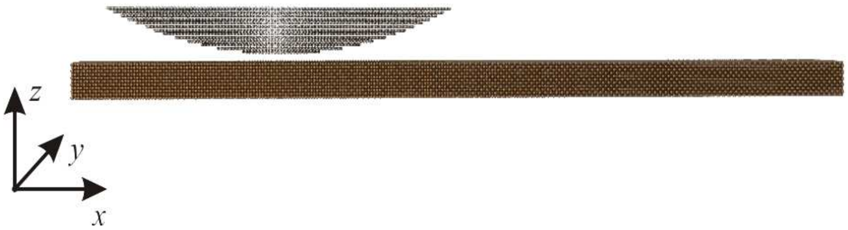

Figure 3.2: Initial simulation configuration (magnified z-axis)

system can be seen in Figure 3.2.

For our runs, the block is frozen to a depth of 3Å from the bottom (xy) and lateral (xz and yz) walls. The rigidly translated atoms of the stylus occupy its topmost 8Å. We apply a thermostat to the non-frozen part of the system, with a target temperature of 300K.

We chose the softer metal for the stylus to limit the extent of the deformation region laterally. The system is quite narrow in the y direction and we tried to avoid deformations due to stylus penetration being affected by the frozen sides of the block. In larger simulation volumes, a hard stylus on soft block may be realized.

Two runs have been completed with this system. Their difference was the horizontal speed at which the stylus moved and the prescribed vertical force between the surfaces. In the first simulation, we chose a sliding velocity of $v_{s,1} = 100\text{m/s}$ and a normal force $P_1 = 2 \cdot 10^{-12}\text{N}$. In the second simulation, the respective parameters were $v_{s,2} = 200\text{m/s}$ and $P_2 = 5 \cdot 10^{-11}\text{N}$.

To find the pressure these forces correspond to, we have to calculate the surface area of the top of the stylus (see Figure 3.3). Since the width and height of the system are smaller than the radius of the stylus, this area will be:

$$A = A_1 + A_2 + A_3 = 2A_1 + A_2 \Rightarrow$$

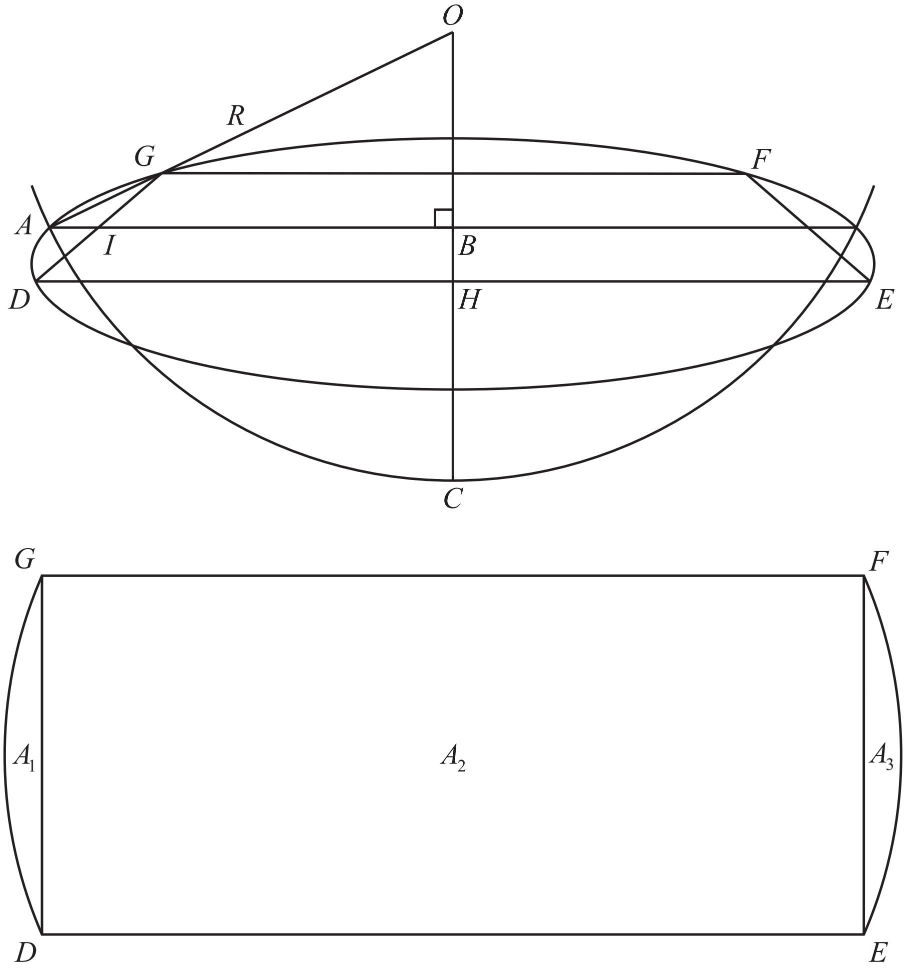

Figure 3.3: Stylus tip geometry. Side and top views

$$A = 2\int_{IB}^{AB} DG dx + A_2 = 2\int_{DH}^{AB} 2\sqrt{BD^2 - BI^2} dx + A_2 \Rightarrow$$

$$A = 4\int_{DH}^{AB} \sqrt{AB^2 - DH^2} dx + A_2$$

$$A = AB^2 \left[\pi - \sin\left(2\sin^{-1}\left(\frac{DH}{AB}\right)\right) - 2\sin^{-1}\left(\frac{DH}{AB}\right)\right] + GD \cdot DE \tag{3.2}$$

where:

$$AB = \sqrt{R^2 - (R - BC)^2} = \sqrt{R^2 - [R - (L_z - h - d)]^2}$$

$$DH = \sqrt{DB^2 - BH^2} = \sqrt{AB^2 - \left(\frac{GD}{2}\right)^2}$$

$$GD = L_y - 2d_y$$

and

$$DE = 2DH$$

where $d_y = 0.5$nm is a small clearance on each side of the stylus in the y direction. For our setup, the area calculated is $A = 1.22 \cdot 10^{-16}\text{m}^2$, leading to pressures $p_1 = 16.4$kPa and $p_2 = 0.41$MPa for the slow and fast run respectively. Both of these pressures are very small compared to the yield pressures of our materials (cf. section 3.1.2), but these were test runs, not intended to stress the system.

The measurements of external sliding forces and the resulting values for the coefficient of friction appear in Figure 3.4 for the slow run. We observe the stylus approaching the block, until a cold weld between the two starts forming (Figure 3.5(a)). The welding area grows (Figure 3.5(b)), pulling the stylus ever stronger on the block, as seen on our measurements for the first $\approx 6 \cdot 10^4$ steps. Deformation of both objects ensues and the resultant picture resembles two growing, opposing wedges (Figure 3.5(c)). The wedges tend to push the objects apart, which increases

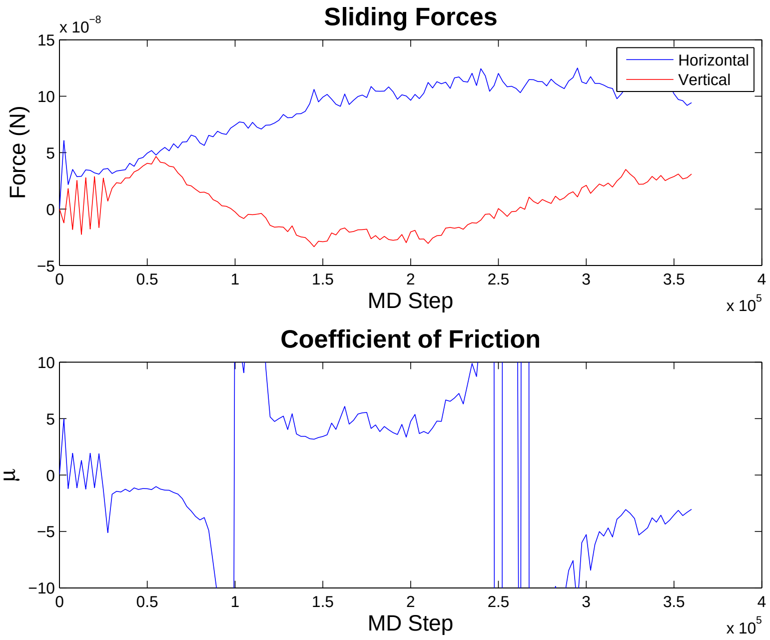

Figure 3.4: Sliding forces and coefficient of friction for $v_{s,1} = 100\text{m/s}$ and $P_1 = 2 \cdot 10^{-12}\text{N}$. MD step set at $0.5 \cdot 10^{-15}\text{s}$.

the normal force, as it can be seen between $\approx 6\cdot10^4$ and $\approx 1.3\cdot10^5$ steps. A period of stability follows, and is reflected on both the individual force measurements and the derived coefficient of friction ($\mu \approx 5$, consistent with experiments in non-oxidizing environments[8]), up to approximately $2.1\cdot10^5$ steps. During that time, the cold weld seems to be moving slower than the stylus and left behind. With more deformation, particles get smeared to the xz sides of the simulation volume, where they remain fixed, due to the freezing boundary conditions there (Figure 3.5(d)). For our analysis and quantitative results, we will focus on the measurements before that point.

The measurements of external sliding forces and the resulting values for the coefficient of friction appear in Figure 3.6 for the fast run. As in the case of the slow run, the stylus is lowered, until the formation of a cold weld begins (Figure 3.7(a)) and a pull between the two objects develops along with it (Figure 3.7(b)), between $\approx 8.5\cdot10^4$ and $\approx 10^5$ steps. The deformation of both surfaces leads to the buildup of pressure at the contact for the following $\approx 5\cdot10^4$ steps, returning the measured normal force to approximately zero. However, the wedges observed in the slow case do not appear so clearly here (Figure 3.7(c)). For the next $\approx 5\cdot10^4$ steps the force measurements level off, although the value of the normal force is so small, that no coefficient of friction can really be reported. The stylus seems again to leave behind the cold weld during that interval. Beyond that point, the smearing of the stylus on the side walls (Figure 3.7(d)) appears as in the case of the slow run. We will focus on quantitative data before that point.

In analyzing this data, the first thing we note is that the prescribed normal force has little effect on the runs. The main reason for this is the limit of $v_z = 0.3\text{m/s}$ we set to the rate of vertical motion, for the rigidly translated top of the stylus. This speed is three orders of magnitude lower than the horizontal sliding rate of

(a) Initialization of a cold weld

(b) Fully developed cold weld

(c) Mutual deformation of the two bodies

(d) Stylus smearing on the side walls

Figure 3.5: Slow run snapshots (magnified z-axis)

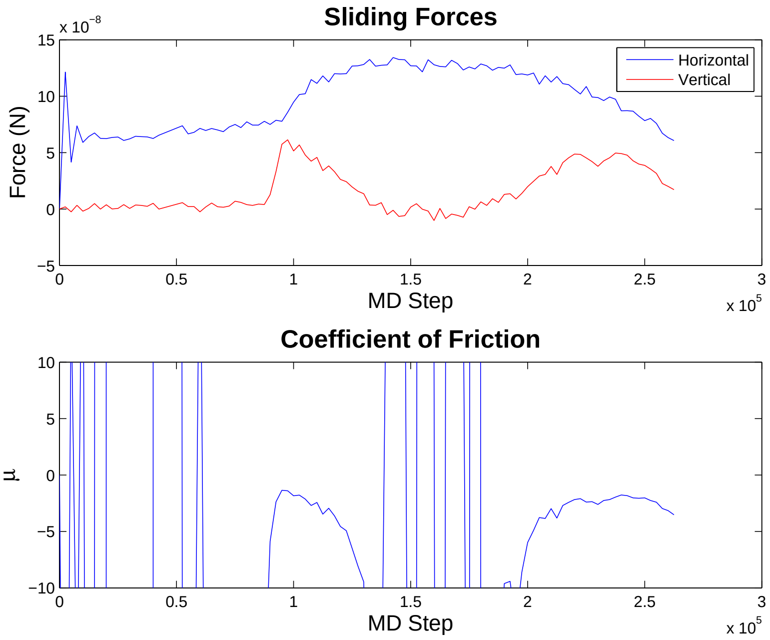

Figure 3.6: Sliding forces and coefficient of friction for $v_{s,2} = 200\text{m/s}$ and $P_2 = 5 \cdot 10^{-11}\text{N}$. MD step set at $0.5 \cdot 10^{-15}\text{s}$.

(a) Initialization of a cold weld

(b) Fully developed cold weld

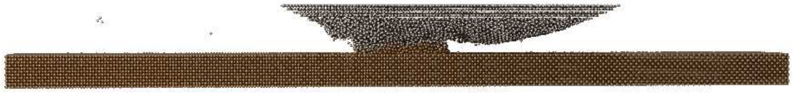

(c) Mutual deformation of the two bodies

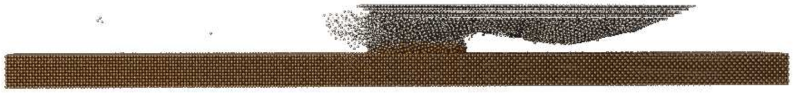

(d) Stylus smearing on the side walls

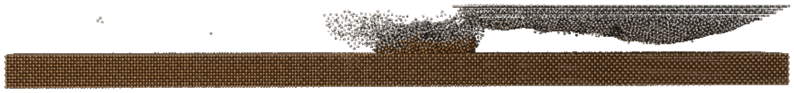

(e) End of run

Figure 3.7: Fast run snapshots (magnified z-axis)

either run. Thus, the reaction of the normal force feedback to the conditions at the contact was severely handicapped. The small v_z value was chosen to allow the stylus to respond to the motion of its top without exerting inertial resistance much higher than the prescribed normal force. Such excess would lead to a vertical motion reversal and subsequent oscillations. Oscillations are still evident in the normal force measurements in the beginning of both runs, but there is a net downward motion. While the rate limit of vertical motion will be increased in runs close to the calculated yield strengths of the materials, it does not detract significantly from the realism of the present calculations. The slowly responding top would correspond to the inertial behavior of a larger surface, of which the asperity is but a small part. In such cases, we expect most contacts to be stressed to the yield strength, but, as the surface is dynamically reshaped, some asperities will be forced into contact with protrusions on the opposite surface, while others will break contact, or even detach from the surface.

Another observation that can be made regards the qualitative similarity of the two runs, even in the region where side wall smearing makes our data suspect. The strong adhesive force between the two objects manifests itself as a positive normal force in our measurements (which are of the external force that would be required on the stylus), as the stylus approaches the block. This attractive force leads to the cold welds that have also been described in physical experiments. The actual formation and growing of the weld is marked by a steady increase of the horizontal force, as the motion of the stylus produces plastic deformation on both bodies. The following period of stability is remarkable for the consistency of the horizontal force measurements ($\approx 1.2 \cdot 10^{-8}$N) between the two runs, despite the significant disparity in normal forces and the qualitative differences in the deformation of the two objects.

As the oncoming break of the contact appears to be happening within the softer, aluminum stylus body, we may deduce that it is indeed the plastic properties of that material that determine the horizontal friction force at a contact, in accordance with theory.

Another agreement with theory comes at the level of the plateau reached by the normal force in the slow run. At $\approx -3 \cdot 10^{-8}$N, it corresponds to the value obtained by the yield strength of aluminum over the area of the stylus top. It is during this plateau also, that the value for the coefficient of friction stabilizes around 5. This is a very important agreement with existing experimental data. Values of 4 or 5 for the coefficient of friction are reported by Bowden and Tabor in [8] for clean metallic surfaces in a non-oxidizing atmosphere (H_2 or N_2).

The shorter and less distinct plateau of the normal force for the fast run does not yield such theory conforming results. While more experimentation is needed, it can be argued that the inertia and hardness of the block, protect its surface from extreme deformations and the piling up of material, that raised the normal pressure to the yield strength in the slow case. This effect would lead to an increase of the coefficient of friction with velocity. Specifically, some of the contacts between the two surfaces would be exerting drag, without causing the deformations that would make them load-bearing. As a result, the effective contact area between the sliding surfaces, and by extension the frictional force, would be increased above the plastic flow predictions ($A = P/p_m$ and $S = \mu P$ respectively). It remains up to future experiments to verify the effect and characterize its dependence on velocity. That the normal force plateau in the 100m/s slide was at the theoretical limit and in the 200m/s slide practically at zero may indicate that there is a critical speed, where there is an abrupt change in the frictional behavior.

3.3 Molecular Dynamics with Electrodynamics

3.3.1 Electrical Fuse

Our first experiments with full code functionality were intended as verifications of the physical validity of the latter. A simple setup to that end is that of an electrical fuse. It consists of two metal plates at the top and bottom of the volume, where voltage is applied. The plates are connected with a straight wire of the same material. This setup lends itself to a basic check of Ohm's law, through the measurement of the current in the wire. It also allows us to check the integration between electrodynamics and molecular dynamics in the evolution of the ohmically heated wire.

The specific system is enclosed in a computational volume with dimensions: $L_x = L_y = 4.047\text{nm}$ and $L_z = 6.8799\text{nm}$. The plates have a depth $h = 8.094\text{Å}$ and the wire a radius $R_w = 6\text{Å}$. The material in this simulation is aluminum. A potential difference $\Delta V = 0.1\text{V}$ is applied between the top and bottom of the system, after an initial thermalization to a temperature of $T_i \approx 230K$. In terms of the numerics, molecular dynamics progresses with a time step $\Delta t_{MD} = 0.5 \cdot 10^{-15}\text{s}$, while electrodynamics utilizes a time step $\Delta t_{ED} = 10^{-20}\text{s}$ and cubic cells of side $d = 4.047\text{Å}$.

In this system, and if we ignore the spreading resistance at the junctions between the wire and the plates, we can calculate a current density $J_c = 6.96 \cdot 10^{14}\text{A/m}^2$ in the wire. The numerical result of a maximum current density $J_n = 6.6 \cdot 10^{14}\text{A/m}^2$ is only 5% away from that estimate. Given this current density, ohmic heating causes the temperature of the system to rise. We chose to apply a potential difference that would bring the wire to its boiling point within a very short time ($\approx$ 1ps). The intention was both to keep this test run short and to see a more pronounced feedback between MD and ED, as the wire explodes and the connection is severed. Given a conductivity $\sigma_{Al}^{300K} = 3.66 \cdot 10^7 \mathrm{S/m}$ for aluminum, the power deposited on the wire is:

$$P_{Ohm} = \frac{J_c^2}{\sigma_{Al}^{300K}} V_w = \frac{J_c^2}{\sigma_{Al}^{300K}} \pi R_w^2 \left(L_z - 2h\right)$$

or $P_{Ohm} = 7.88 \cdot 10^{-5}\mathrm{W}$. There is no heatsink in the system, therefore this power will serve to raise its temperature. If we eliminate $h_f = 2.024\text{Å}$ at the top and bottom of the system, that we keep frozen, we can calculate the rate of this rise as:

$$\frac{dT}{dt} = \frac{P_{Ohm}}{c_{Al}^{298K} V_{syst}} = \frac{P_{Ohm}}{c_{Al}^{298K} \left[V_w + 2L_x L_y (h - h_f)\right]}$$

where, for $c_{Al}^{298K} = 24.2\mathrm{J/(mol \cdot K)} \approx 2.42 \cdot 10^6 \mathrm{J/(m^3 \cdot K)}$, we find a temperature rise rate $dT/dt = 1.26 \cdot 10^{15}\mathrm{K/s}$. Our measurements, do indeed adhere to this rate in the beginning (cf. Figure 3.8). As the temperature rises, the experiment deviates from our predictions, mainly because heat has not enough time to distribute evenly across the system and the temperature around the center of the wire rises faster than the average. Near the end of the run, the deviation is also due to the fact that the wire is disintegrating (its density drops and the conductivity follows), allowing less current to pass and therefore less power deposited.

That heat is trapped in the wire, is indeed evident in the snapshots of the system. At the beginning of the run (see Figure 3.9), after the thermalization has brought the temperature of the system to T_i, the material maintains its crystalline structure and current density is higher along the wire, while the bending of the current density field around the junctions is evident. As the simulation progresses, and while still below the melting point of aluminum (see Figure 3.10), the material of the wire has clearly lost its periodic structure, as opposed to that of the plates and

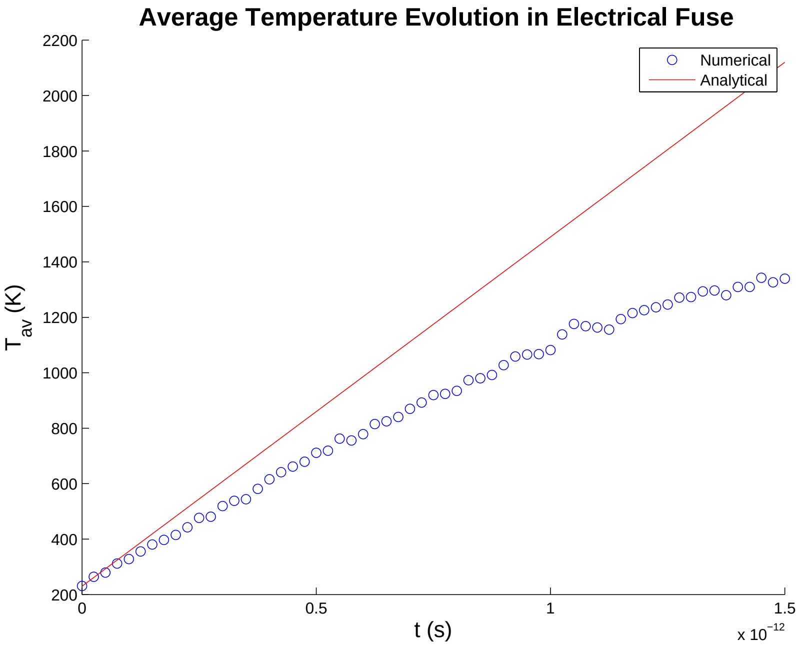

Figure 3.8: Electrical fuse temperature evolution

it has started deforming. The next two snapshots (Figures 3.11 and 3.12) effectively show the wire exploding, while evidence of significant heat diffusion to the plates is only clear near the end of the simulation.

3.3.2 Sliding Experiments

Our sliding experiments are currently in progress. We are repeating the previous fast and slow slide runs, as well as static runs, in slightly larger systems, with and without electrodynamics, and with and without motion of the top of the stylus in the vertical direction. On the electrodynamics front, we had calculated the limit for melting due to currents to be ≈ 35mV, for the applied potential difference. We have chosen a value of 20mV, so that we are close to but not at the melting point of our materials. As far as the speed limit for the normal force feedback is concerned, the determining factor is to avoid exceeding the yield strength of Aluminum, with our adjustments. For a quick estimate, we used the Rose potential for Al and found that a vertical displacement of $\approx 4 \cdot 10^{-3}$A, between the handled top of the stylus and its underlying volume, would bring us close to the yield strength of the material. Division by the simulation time step ($0.5 \cdot 10^{-15}$s) yields a speed limit of ≈ 800m/s, for the normal force feedback mechanism. We have taken a conservative approach and limited that velocity further, to 10m/s. Pictures from the slow and fast versions, with electrodynamics enabled but no force feedback for the vertical motion, are shown in Figure 3.13 and Figure 3.14 respectively.

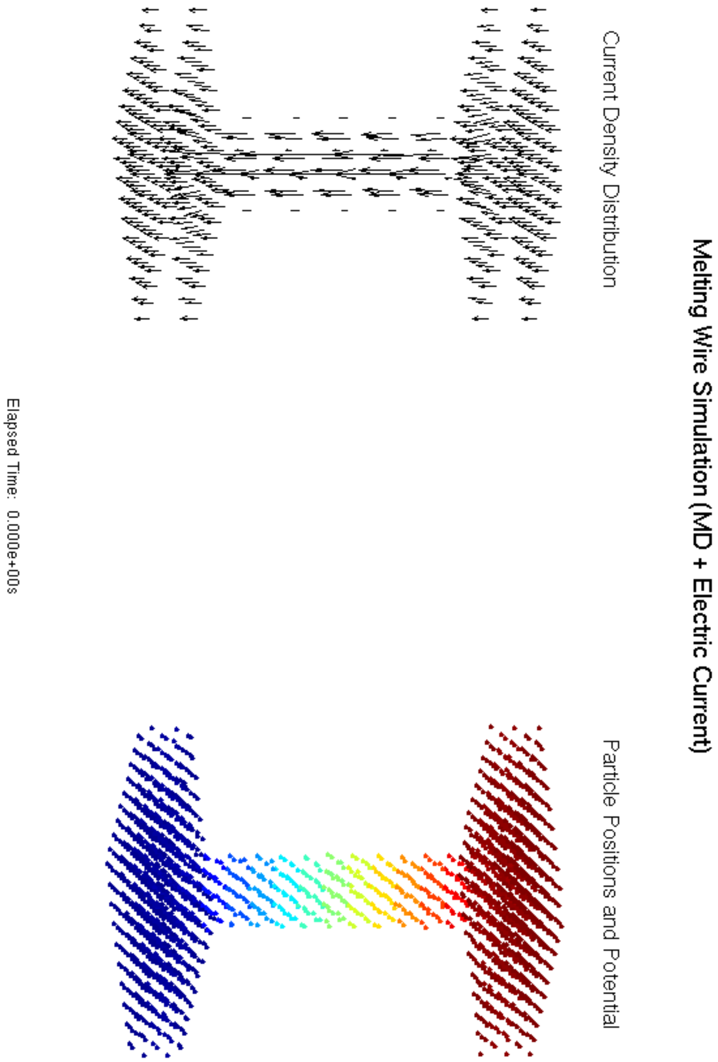

Figure 3.9: Thermalized fuse ($T_{av} \approx 230$K). Color code indicates voltage.

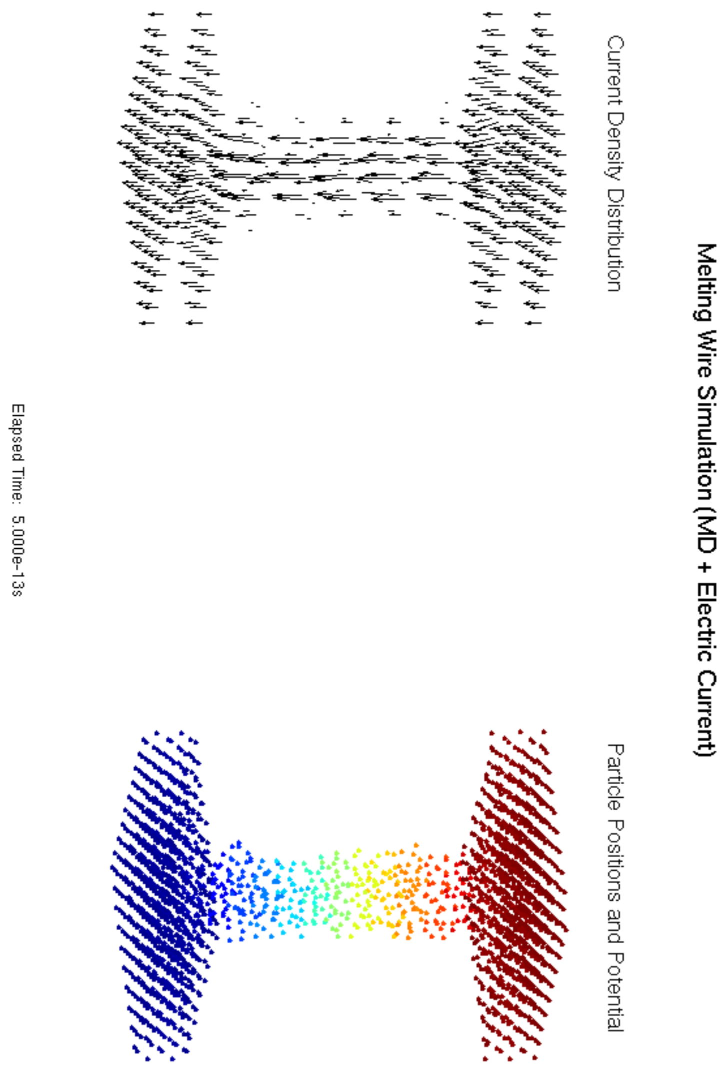

Figure 3.10: Fuse at $t = 0.5 \cdot 10^{-12}$s ($T_{av} \approx 710$K). Color code indicates voltage.

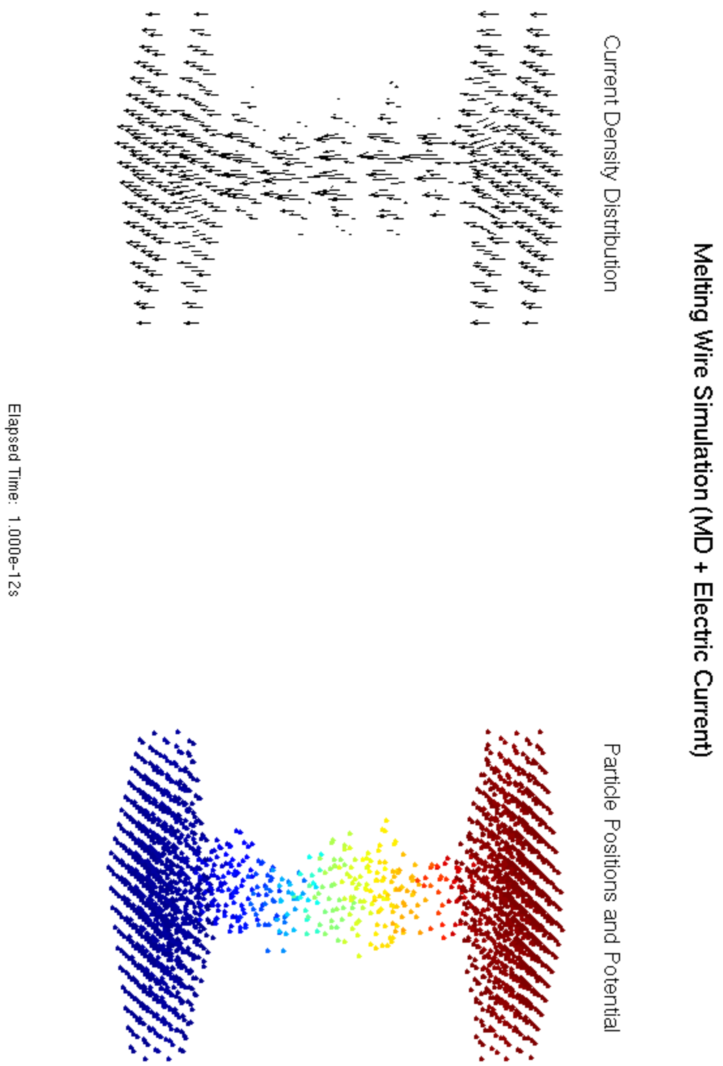

Figure 3.11: Fuse at $t = 1 \cdot 10^{-12}$s ($T_{av} \approx 1080$K). Color code indicates voltage.

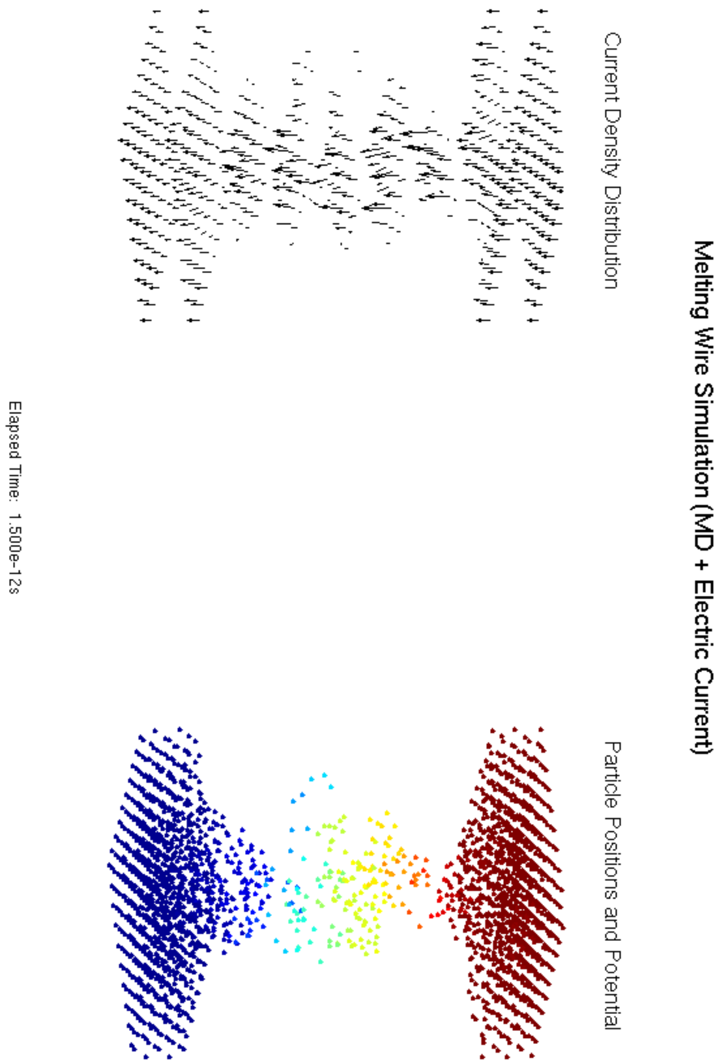

Figure 3.12: Fuse at $t = 1.5 \cdot 10^{-12}$s ($T_{av} \approx 1340$K). Color code indicates voltage.

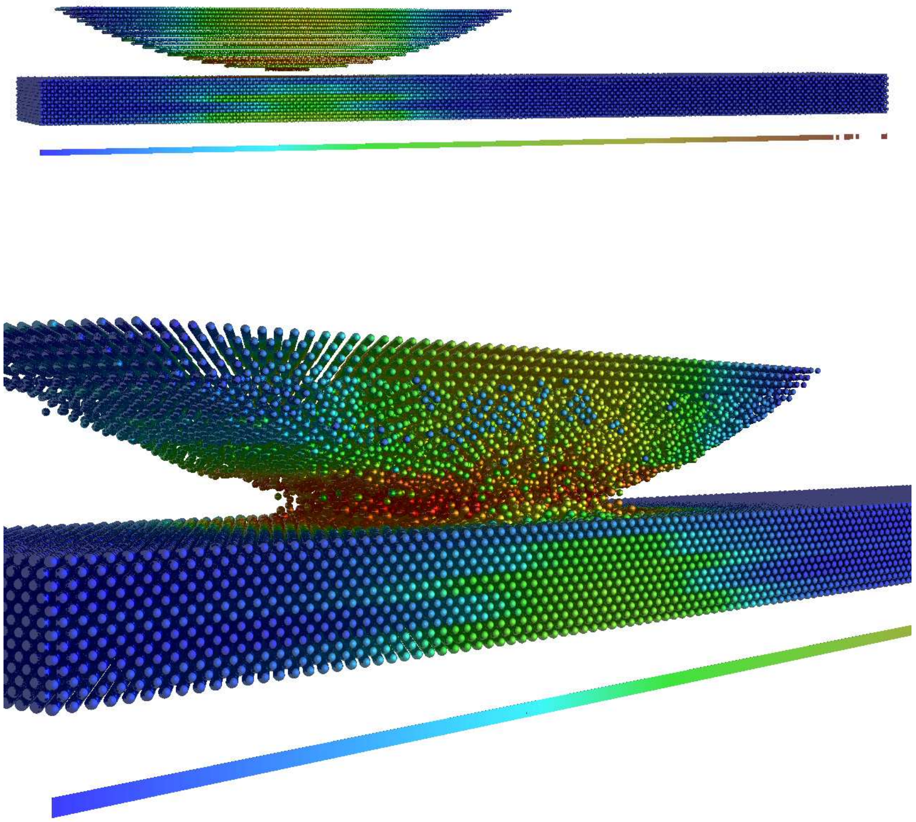

Figure 3.13: Slow run simulations. Color scale corresponds to current density.

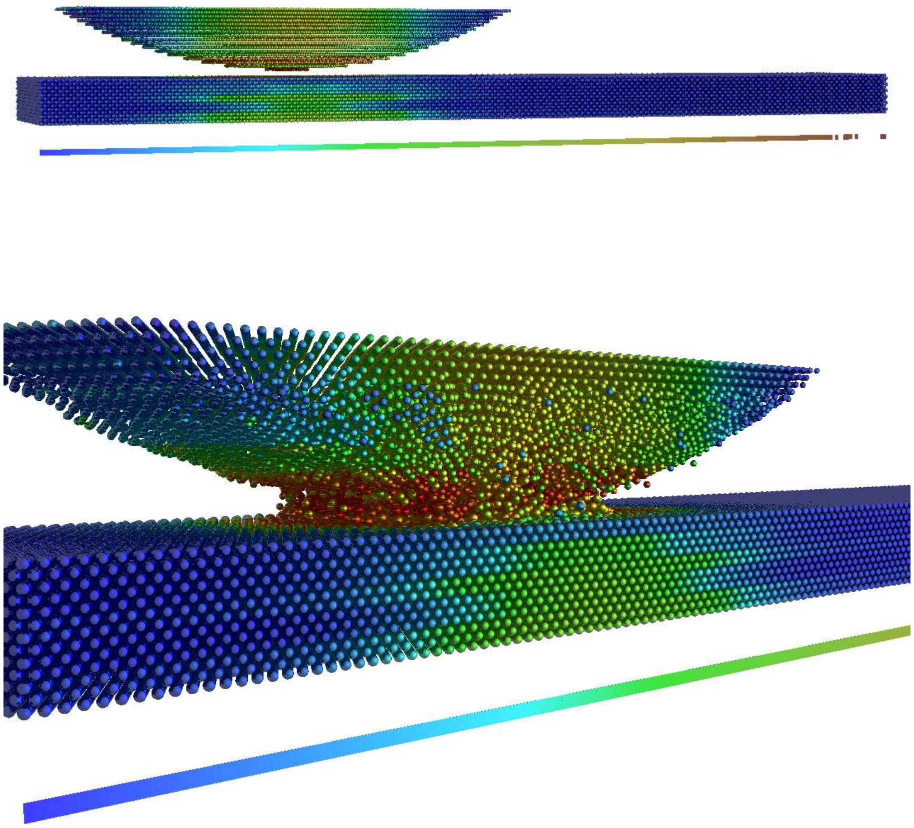

Figure 3.14: Fast run simulations. Color scale corresponds to current density.

Chapter 4

Conclusions

There are two general accomplishments of this work so far. On the one hand, it has produced a versatile tool for the study of metallic friction. On the other hand, through its first results, it has provided insight into a mechanism that may explain, on its own or as part of a set, a velocity dependence of the coefficient of friction for metals.

The development of the tool involved first of all the modification of the existing HOLA molecular dynamics (MD) code. To that end, we have utilized a combination of the MEAM and Rose potentials, to calculate the interactions between atoms. Furthermore, we have developed code, to perform slider-on-block experiments. The operating scheme is that the bottom and sides of the block are held fixed, while the top of the slider is rigidly moved. In the direction parallel to the surface of the block, we move the slider top at a prescribed, constant velocity. In the perpendicular direction, the motion of the slider top is either arrested or determined by a feedback loop, that attempts to attain and hold a target loading force between the two objects. That force, as well as the frictional force, are measured through the reactive force on the rigidly translated, slider top particles from the rest of the slider volume.

The other basic part of the tool that is required, is the electrodynamic (ED) solver that will allow us to study the behavior of the system, when it acts as both a mechanical and an electrical contact. The major obstacle that has been cleared here was due to the much shorter timescales involved in the ED calculations. Specifically, we found that the necessary time step for the ED calculations is 5 orders of magnitude shorter than the MD time step. Moving the whole code to such a time step would make simulations impractical. Instead, we consider the atomic configuration produced by each MD step the stage, for the development of an ED equilibrium. Solving this problem with an iterative method leads to fast convergence and reduces the simulation speed to ≈ 0.5 of the MD-only case, instead of $\approx 10^{-5}$. Although currently the code doesn't handle magnetic fields, the solver framework is general enough that such capabilities can be added. Furthermore, by treating valence electrons and the atoms they belong to as independent carriers of charge, we can study the direct electromagnetic force effects on the atoms comprising our system.

Compared with the work by the groups of M. Robbins and D. W. Brenner, our code and simulations offer unique perspectives on the problem of friction. Luan and Robbins[18, 19] do not deal with electrodynamics. They use generic materials and simple pairwise potentials throughout the simulation volume. Their focus is on the basic properties and the merits of the atomistic versus the continuum approach. They also consider one of the two objects rigid, while we place no restriction on the evolution of either the slider or the block. Brenner's group studies the same materials as we do and they do include electrodynamic considerations, but only in the form of Joule heating, potentially missing the interaction between charged atoms and electromagnetic fields, which is available to our approach.

Of course, every numerical code is only as good as it is realistic in its rendition of the physical world. Beyond coding the right equations into a code, we should therefore be able to reproduce established physical results, before moving into uncharted territory. In this respect, our first, MD-only results (cf. section 3.2) are extremely encouraging. As we have seen in our measurements from the slow (100m/s) run (see Figure 3.4), the freely evolving normal force in this experiment encounters an upper limit, consistent with the experimental yield strength of aluminum, the softer material in our system. Furthermore, the corresponding coefficient of friction, of ≈ 5, is consistent with the measurements presented by Bowden and Tabor[8] for other clean metallic surfaces in a non-oxidizing atmosphere, which were between 4 and 5. The agreement in the friction coefficient is particularly encouraging, in light of the work of Luan and Robbins[18, 19], where continuum mechanics simulations of asperities are criticized for getting stresses right within a small factor, but failing in the coefficient of friction by an order of magnitude or more.

The qualitative agreement of our experiments with established results is also very good. Cold welds are evident in all our friction runs, consistent with post-mortem observations and the importance attributed to adhesion by Bowden and Tabor. Furthermore, plastic deformation accompanies the evolution of the contact. The most extensive deformation occurs in the weaker object, within which the break of the contact also seems to happen, again in accordance with the experimental observations.

On the electrodynamic front, validation of the code comes from the analysis of the electric fuse simulation (cf. section 3.3.1). Both the current through the wire in that system and the rate of temperature increase are consistent with theory. In qualitative terms, electric current patterns, in both that problem and the first snapshots of our ED enabled slider experiments, are in agreement with physical intuition, by showing concentration and consequent high values of current density where the cross section of the current path narrows.

Beyond their agreement with theory and previous work, our first experiments provide a glimpse at new physical mechanisms, that could account, at least in part, for a velocity dependence of the metallic coefficient of friction. This can be seen when comparing the slow and fast, MD-only run measurements (confer Figures 3.4 and 3.6). In both cases, the starting configuration is the same and we effectively hold the height of the slider top fixed. The situation would correspond to an asperity between two surfaces that are already supported at other contact points. As the two runs evolve, the asperity develops a cold weld and a frictional force of approximately the same magnitude in both cases. However, the normal force graphs are distinctly different. In the 100m/s run the two materials form obvious, mating wedges, that push them apart and raise the normal pressure to the yield strength of the weaker. In the 200m/s run on the other hand, the wedges are less pronounced and their only effect is to provide enough repulsion to neutralize the adhesive force and bring the total normal force at the top of the stylus to zero. If we zoom out on the picture of a surface supported on many asperities, it is clear that, in the first case, we will have a load-bearing contact spontaneously created and relieving neighboring ones. In the second case, many contacts can be created, beyond the ones supporting the surfaces. In the fast case then, the dependence of the frictional force on the contact area is still valid, but the proportionality between normal force and contact area no longer holds, as non load bearing contacts are feasible. Assuming that eq. (1.3) still holds:

$$S = sA$$

and because now the contact pressure does not obey eq. (1.2) anymore, but:

$$P < p_m A$$

the coefficient of friction:

$$\mu = \frac{S}{P}$$

can be expected to increase at high velocities.

Appendix A

Atomic Potential Force Calculation

Given the energy E of the system, the force $\vec{f}_m$ acting on particle m will be:

$$\vec{f}_m = \frac{dE}{d\vec{R}_m} = \sum_i \frac{dE_i}{d\vec{R}_m} \Rightarrow$$

$$f_m^\eta = \sum_i \frac{\partial E_i}{\partial R_m^\eta} \tag{A.1}$$

This expression can be calculated numerically with a simple finite differences algorithm, but it is very costly, since it requires the calculation of the total system energy seven times per particle. In our implementation, we use such a method only as a validation tool, for the implementation of the analytical solution of eq. (A.1), that follows. Because of the linear form of eq. (A.1), the contributions of the Rose potential and the Modified Embedded Atom Method to the force are additive and can be studied separately.

A.1 Rose potential

If we substitute eq. (2.4) into eq. (A.1):

$$f^{\eta}_{R,m} = \sum_{i} \sum_{j(species(j) \neq species(i))} \left(\frac{\partial S_{ij}}{\partial R^{\eta}_{m}} E_{R,ij} + S_{ij} \frac{\partial E_{R,ij}}{\partial R^{\eta}_{m}} \right)$$

where, according to eq. (2.1):

$$\frac{\partial E_{R,ij}}{\partial R^{\eta}_{m}} = \frac{\partial E_{R,ij}}{\partial a^{*}_{ij}} \frac{\partial a^{*}_{ij}}{\partial R^{\eta}_{m}} = E_{c,ij} a^{*}_{ij} e^{-a^{*}_{ij}} \frac{\partial a^{*}_{ij}}{\partial R^{\eta}_{m}}$$

and, given eq. (2.2):

$$\frac{\partial a^{*}_{ij}}{\partial R^{\eta}_{m}} = -\left(\delta_{im} - \delta_{jm}\right) \frac{\alpha_{ij}}{r_{e,ij}} u^{\eta}_{ij}$$

$\frac{\partial S_{ij}}{\partial R^{\eta}_{m}}$ will be derived in section A.3.

A.2 MEAM

Specifically, if we substitute $E_{M,i}$ from eq. (2.6):

$$f^{\eta}_{M,m} = \sum_{i} \left[\frac{\partial F_i}{\partial R^{\eta}_{m}} + \frac{1}{2} \sum_{j(\neq i)} \left(\frac{\partial S_{ij}}{\partial R^{\eta}_{m}} \Phi_{ij} + S_{ij} \frac{\partial \Phi_{ij}}{\partial R^{\eta}_{m}} \right) \right] \tag{A.2}$$

Let us calculate each one of the terms in this equation.

A.3 $\frac{\partial S_{ij}}{\partial R^{\eta}_{m}}$

From eq. (2.19):

$$\frac{\partial S_{ij}}{\partial R^{\eta}_{m}} = \sum_{l(\neq i,j)} \left(\frac{\partial S_{ilj}}{\partial R^{\eta}_{m}} \prod_{k(\neq i,j,l)} S_{ikj} \right)$$

or,

$$\begin{aligned}\frac{\partial S_{ij}}{\partial R_m^\eta} &= \delta_{im}\sum_{l(\neq i,j)}\left(\frac{\partial S_{ilj}}{\partial R_i^\eta}\prod_{k(\neq i,j,l)}S_{ikj}\right)+\\ &+ \delta_{jm}\sum_{l(\neq i,j)}\left(\frac{\partial S_{ilj}}{\partial R_j^\eta}\prod_{k(\neq i,j,l)}S_{ikj}\right)+\\ &+ (1-\delta_{im})(1-\delta_{jm})\frac{\partial S_{imj}}{\partial R_m^\eta}\prod_{k(\neq i,j,m)}S_{ikj}\end{aligned}$$

For the range of x_{ikj} values where g_c (from eq. (2.24)) is not a constant, we can generally write:

$$\frac{\partial S_{ikj}}{\partial R_m^\eta}=\frac{\partial S_{ikj}}{\partial x_{ikj}}\frac{\partial x_{ikj}}{\partial R_m^\eta}=8(1-x_{ikj})^3\left[1-(1-x_{ikj})^4\right]\frac{\partial x_{ikj}}{\partial R_m^\eta}$$

where, given the implied definition of eq. (2.23):

$$\frac{\partial x_{ikj}}{\partial R_m^\eta}=\frac{\partial x_{ikj}}{\partial C_{ikj}}\frac{\partial C_{ikj}}{\partial R_m^\eta}=\frac{1}{C_{max,ikj}-C_{min,ikj}}\frac{\partial C_{ikj}}{\partial R_m^\eta}$$

From eq. (2.20):

$$\frac{\partial C_{ikj}}{\partial R_m^\eta}=\frac{\partial C_{ikj}}{\partial X_{ik}}\frac{\partial X_{ik}}{\partial R_m^\eta}+\frac{\partial C_{ikj}}{\partial X_{kj}}\frac{\partial X_{kj}}{\partial R_m^\eta}$$

where:

$$\frac{\partial C_{ikj}}{\partial X_{ik}}=\frac{2-4\left(X_{ik}-X_{kj}\right)-2\left(X_{ik}-X_{kj}\right)^2+4\left(X_{ik}^2-X_{kj}^2\right)}{\left[1-\left(X_{ik}-X_{kj}\right)^2\right]^2}$$

and:

$$\frac{\partial C_{ikj}}{\partial X_{kj}}=\frac{2+4\left(X_{ik}-X_{kj}\right)-2\left(X_{ik}-X_{kj}\right)^2-4\left(X_{ik}^2-X_{kj}^2\right)}{\left[1-\left(X_{ik}-X_{kj}\right)^2\right]^2}$$

finally, from eqns. (2.21) and (2.22):

$$\frac{\partial X_{ik}}{\partial R_m^\eta} = \frac{2}{R_{ij}^2}\left[\delta_{im}\left(R_{ij}^\eta X_{ik} - R_{ik}^\eta\right) - \delta_{jm}R_{ij}^\eta X_{ik} + \delta_{km}R_{ik}^\eta\right]$$

and:

$$\frac{\partial X_{kj}}{\partial R_m^\eta} = \frac{2}{R_{ij}^2}\left[\delta_{im}R_{ij}^\eta X_{kj} - \delta_{jm}\left(R_{ij}^\eta X_{kj} - R_{kj}^\eta\right) - \delta_{km}R_{kj}^\eta\right]$$

A.4 $\frac{\partial F_i}{\partial R_m^\eta}$

From eq. (2.7):

$$\frac{\partial F_i}{\partial R_m^\eta} = \frac{\partial F_i}{\partial \bar{\rho}_i}\frac{\partial \bar{\rho}_i}{\partial R_m^\eta} = \frac{A_i E_{c,i}}{\bar{\rho}_i^0}\left[ln\left(\frac{\bar{\rho}_i}{\bar{\rho}_i^0}\right) + 1\right]\frac{\partial \bar{\rho}_i}{\partial R_m^\eta}$$

Given eq. (2.13):

$$\begin{aligned}\frac{\partial \bar{\rho}_i}{\partial R_m^\eta} &= \frac{2}{1+e^{-\Gamma_i}}\frac{\partial \rho_i^{(0)}}{\partial R_m^\eta} + \\ &+ \left[\frac{\partial \Gamma_i}{\partial\left(\rho_i^{(0)}\right)^2}\frac{\partial\left(\rho_i^{(0)}\right)^2}{\partial R_m^\eta} + \frac{\partial \Gamma_i}{\partial\left(\rho_i^{(1)}\right)^2}\frac{\partial\left(\rho_i^{(1)}\right)^2}{\partial R_m^\eta} + \right. \\ &+ \left.\frac{\partial \Gamma_i}{\partial\left(\rho_i^{(2)}\right)^2}\frac{\partial\left(\rho_i^{(2)}\right)^2}{\partial R_m^\eta} + \frac{\partial \Gamma_i}{\partial\left(\rho_i^{(3)}\right)^2}\frac{\partial\left(\rho_i^{(3)}\right)^2}{\partial R_m^\eta}\right]\frac{2\rho_i^{(0)}e^{-\Gamma_i}}{(1+e^{-\Gamma_i})^2}\end{aligned}$$

where, according to eq. (2.14):

$$\frac{\partial \Gamma_i}{\partial\left(\rho_i^{(0)}\right)^2} = -\frac{\Gamma_i}{\left(\rho_i^{(0)}\right)^2}$$

$$\frac{\partial \Gamma_i}{\partial \left(\rho_i^{(1)}\right)^2} = \frac{t_i^{(1)}}{\left(\rho_i^{(0)}\right)^2}$$

$$\frac{\partial \Gamma_i}{\partial \left(\rho_i^{(2)}\right)^2} = \frac{t_i^{(2)}}{\left(\rho_i^{(0)}\right)^2}$$

$$\frac{\partial \Gamma_i}{\partial \left(\rho_i^{(3)}\right)^2} = \frac{t_i^{(3)}}{\left(\rho_i^{(0)}\right)^2}$$

while, from eq. (2.8):

$$\frac{\partial \rho_i^{(0)}}{\partial R_m^\eta} = \sum_{j(\neq i)} \left(\frac{\partial S_{ij}}{\partial R_m^\eta} \rho_j^{a(0)} + S_{ij} \frac{\partial \rho_j^{a(0)}}{\partial R_m^\eta} \right)$$

and:

$$\frac{\partial \left(\rho_i^{(0)}\right)^2}{\partial R_m^\eta} = 2\rho_i^{(0)} \frac{\partial \rho_i^{(0)}}{\partial R_m^\eta}$$

Similarly, from eq. (2.9):

$$\begin{aligned} \frac{\partial \left(\rho_i^{(1)}\right)^2}{\partial R_m^\eta} &= 2\sum_\alpha \left(\sum_{j(\neq i)} u_{ij}^\alpha S_{ij} \rho_j^{a(1)} \right) \sum_{j(\neq i)} \left[u_{ij}^\alpha \frac{\partial S_{ij}}{\partial R_m^\eta} \rho_j^{a(1)} + u_{ij}^\alpha S_{ij} \frac{\partial \rho_j^{a(1)}}{\partial R_m^\eta} + \right. \\ &+ \left. (\delta_{im} - \delta_{jm}) \frac{u_{ij}^\alpha u_{ij}^\eta - \delta_{\alpha\eta}}{R_{ij}} S_{ij} \rho_j^{a(1)} \right] \end{aligned}$$

from eq. (2.10):

$$\frac{\partial \left(\rho_i^{(2)}\right)^2}{\partial R_m^\eta} = 2\sum_{\alpha,\beta} \left(\sum_{j(\neq i)} u_{ij}^\alpha u_{ij}^\beta S_{ij} \rho_j^{a(2)} \right) - \frac{1}{3} \left[\sum_{j(\neq i)} S_{ij} \rho_j^{a(2)} \right]^2$$

$$
\begin{aligned}
\frac{\partial\left(\rho_i^{(2)}\right)^2}{\partial R_m^\eta} &= 2\sum_{\alpha,\beta}\left(\sum_{j(\neq i)} u_{ij}^\alpha u_{ij}^\beta S_{ij}\rho_j^{a(2)}\right)\sum_{j(\neq i)}\left[u_{ij}^\alpha u_{ij}^\beta \frac{\partial S_{ij}}{\partial R_m^\eta}\rho_j^{a(2)} + u_{ij}^\alpha u_{ij}^\beta S_{ij}\frac{\partial \rho_j^{a(2)}}{\partial R_m^\eta}+\right.\\
&+ \left.(\delta_{im}-\delta_{jm})\frac{2u_{ij}^\alpha u_{ij}^\beta u_{ij}^\eta - \delta_{\alpha\eta}u_{ij}^\beta - \delta_{\beta\eta}u_{ij}^\alpha}{R_{ij}} S_{ij}\rho_j^{a(2)}\right] -\\
&- \frac{2}{3}\left(\sum_{j(\neq i)} S_{ij}\rho_j^{a(2)}\right)\sum_{j(\neq i)}\left[\frac{\partial S_{ij}}{\partial R_m^\eta}\rho_j^{a(2)} + S_{ij}\frac{\partial \rho_j^{a(2)}}{\partial R_m^\eta}\right]
\end{aligned}
$$

and, from eq. (2.11):

$$
\begin{aligned}
\frac{\partial\left(\rho_i^{(3)}\right)^2}{\partial R_m^\eta} &= 2\sum_{\alpha,\beta,\gamma}\left(\sum_{j(\neq i)} u_{ij}^\alpha u_{ij}^\beta u_{ij}^\gamma S_{ij}\rho_j^{a(3)}\right)\sum_{j(\neq i)}\left[u_{ij}^\alpha u_{ij}^\beta u_{ij}^\gamma \frac{\partial S_{ij}}{\partial R_m^\eta}\rho_j^{a(3)}+\right.\\
&+ u_{ij}^\alpha u_{ij}^\beta u_{ij}^\gamma S_{ij}\frac{\partial \rho_j^{a(3)}}{\partial R_m^\eta}+\\
&+ \left.(\delta_{im}-\delta_{jm})\frac{3u_{ij}^\alpha u_{ij}^\beta u_{ij}^\gamma u_{ij}^\eta - \delta_{\alpha\eta}u_{ij}^\beta u_{ij}^\gamma - \delta_{\beta\eta}u_{ij}^\alpha u_{ij}^\gamma - \delta_{\beta\eta}u_{ij}^\alpha u_{ij}^\beta}{R_{ij}} S_{ij}\rho_j^{a(3)}\right] -\\
&- \frac{6}{5}\sum_{\alpha}\left(\sum_{j(\neq i)} u_{ij}^\alpha S_{ij}\rho_j^{a(3)}\right)\sum_{j(\neq i)}\left[u_{ij}^\alpha\frac{\partial S_{ij}}{\partial R_m^\eta}\rho_j^{a(3)} + u_{ij}^\alpha S_{ij}\frac{\partial \rho_j^{a(3)}}{\partial R_m^\eta}+\right.\\
&+ \left.(\delta_{im}-\delta_{jm})\frac{u_{ij}^\alpha u_{ij}^\eta - \delta_{\alpha\eta}}{R_{ij}} S_{ij}\rho_j^{a(3)}\right]
\end{aligned}
$$

The last four expressions involve derivatives of $\rho_j^{a(h)}$. According to eq. (2.12):

$$
\frac{\partial \rho_j^{a(h)}}{\partial R_m^\eta} = (\delta_{im}-\delta_{jm})\frac{\beta_j^{(h)}}{r_{e,j}}\rho_j^{a(h)}u_{ij}^\eta
$$

A.5 $\frac{\partial \Phi_{ij}}{\partial R_m^\eta}$

From eq. (2.17):

$$\frac{\partial \Phi_{ij}}{\partial R_m^\eta} = \frac{2}{Z_{ij}} \frac{\partial E^u}{\partial R_m^\eta} - \left.\frac{\partial F_i}{\partial \bar{\rho}_j}\right|_{\bar{\rho}_j = Z_{ij}\rho_j^{a(0)}} \frac{\partial \rho_j^{a(0)}}{\partial R_m^\eta} - \left.\frac{\partial F_j}{\partial \bar{\rho}_i}\right|_{\bar{\rho}_i = Z_{ij}\rho_i^{a(0)}} \frac{\partial \rho_i^{a(0)}}{\partial R_m^\eta}$$

where $\frac{\partial E^u}{\partial R_m^\eta}$ was calculated in section A.1 and the other two derivatives were worked out in section A.4.

Bibliography

[1] *CRC Handbook of Chemistry and Physics.* CRC Press, 2008.

[2] M. I. Baskes. Application of the embedded-atom method to covalent materials: A semiempirical potential for silicon. *Phys. Rev. Lett.*, 59(23):2666–, December 1987.

[3] M. I. Baskes. Modified embedded-atom potentials for cubic materials and impurities. *Phys. Rev. B*, 46(5):2727–2742, Aug 1992.

[4] M. I. Baskes, J. E. Angelo, and C. L. Bisson. Atomistic calculations of composite interfaces. *Modelling And Simulation In Materials Science And Engineering*, 2(3A):505–518, May 1994.

[5] M. I. Baskes, J. S. Nelson, and A. F. Wright. Semiempirical modified embedded-atom potentials for silicon and germanium. *Phys. Rev. B*, 40(9):6085–, September 1989.

[6] M.I. Baskes. Determination of modified embedded atom method parameters for nickel. *Materials Chemistry and Physics*, 50(2):152–158, September 1997.

[7] Daniel Floyd Berisford. Experimental investigation of barrel damage mecha-

nisms in electromagnetic railguns. Master's thesis, The University of Texas at Austin, 2004.

[8] F. P. Bowden and D. Tabor. *The Friction and Lubrication of Solids.* Oxford Classic Texts in the Physical Sciences. Oxford University Press, USA, 2001.

[9] Murray S. Daw and M. I. Baskes. Semiempirical, quantum mechanical calculation of hydrogen embrittlement in metals. *Phys. Rev. Lett.*, 50(17):1285–, April 1983.

[10] D. Dowson. *History of Tribology.* Longman, 1979.

[11] S. M. Foiles, M. I. Baskes, and M. S. Daw. Embedded-atom-method functions for the fcc metals cu, ag, au, ni, pd, pt, and their alloys. *Phys. Rev. B*, 33(12):7983–7991, Jun 1986.

[12] M. Frigo and S.G. Johnson. The design and implementation of fftw3. *Proceedings of the IEEE*, 93(2):216–231, 2005.

[13] Dominic John Martin Holland. *Cracks and Atoms.* PhD thesis, The University of Texas at Austin, 1999.

[14] S.Y. Hu, M.I. Baskes, M. Stan, and L.Q. Chen. Atomistic calculations of interfacial energies, nucleus shape and size of [theta]' precipitates in al-cu alloys. *Acta Materialia*, 54(18):4699–4707, October 2006.

[15] D L Irving, C W Padgett, and D W Brenner. Coupled molecular dynamics/continuum simulations of joule heating and melting of isolated copper-aluminum asperity contacts. *Modelling and Simulation in Materials Science and Engineering*, 17(1):015004 (20pp), 2009.

[16] James Matthew Doyle Lane. *A new Continuous Hugoniot Method for the numerical study of shock waves.* PhD thesis, The University of Texas at Austin, 2005.

[17] Byeong-Joo Lee, Jae-Hyeok Shim, and M. I. Baskes. Semiempirical atomic potentials for the fcc metals cu, ag, au, ni, pd, pt, al, and pb based on first and second nearest-neighbor modified embedded atom method. *Phys. Rev. B*, 68(14):144112, Oct 2003.

[18] Binquan Luan and Mark O. Robbins. The breakdown of continuum models for mechanical contacts. *Nature*, 435(7044):929–932, June 2005.

[19] Binquan Luan and Mark O. Robbins. Contact of single asperities with varying adhesion: Comparing continuum mechanics to atomistic simulations. *Physical Review E*, 74(2, Part 2), AUG 2006.

[20] Michael P. Marder. *Condensed Matter Physics.* Wiley, 2000.

[21] IR McNab, E Stefani, M Crawford, M Erengil, C Persad, S Satapathy, H Vanicek, T Watt, and C Dampier. Development of a naval railgun. *IEEE Transactions on Magnetics*, 41(1, Part 2):206–210, JAN 2005.

[22] C. W. Padgett and D. W. Brenner. A continuum-atomistic method for incorporating joule heating into classical molecular dynamics simulations. *Molecular Simulation*, 31(11):749–757, sep 2005.

[23] C. Persad and Z. Castro. Railgun tribology: Characterization and control of multishot wear debris. *IEEE Transactions on Magnetics*, 43(1):173–177, 2007.

[24] William H. Press, Saul A. Teukolsky, William T. Vetterling, and Brian P. Flan-

nery. *Numerical Recipes in C: The Art of Scientific Computing.* Cambridge University Press, Cambridge, New York, 1992.

[25] J. H. Rose, John Ferrante, and John R. Smith. Universal binding energy curves for metals and bimetallic interfaces. *Phys. Rev. Lett.*, 47(9):675–678, Aug 1981.

[26] James H. Rose, John R. Smith, Francisco Guinea, and John Ferrante. Universal features of the equation of state of metals. *Phys. Rev. B*, 29(6):2963–2969, Mar 1984.

[27] Allen Taflove and Susan C. Hagness. *Computational electrodynamics : the finite-difference time-domain method.* Artech House, Boston, 3rd edition, 2005.

[28] Loup Verlet. Computer "experiments" on classical fluids. i. thermodynamical properties of lennard-jones molecules. *Phys. Rev.*, 159(1):98–, July 1967.

[29] Loup Verlet. Computer "experiments" on classical fluids. ii. equilibrium correlation functions. *Phys. Rev.*, 165(1):201–, January 1968.

[30] G. F. Wang, M. A. Van Hove, P. N. Ross, and M. I. Baskes. Monte carlo simulations of segregation in pt-re catalyst nanoparticles. *Journal Of Chemical Physics*, 121(11):5410–5422, September 2004.

[31] Kane Yee. Numerical solution of initial boundary value problems involving maxwell's equations in isotropic media. *Antennas and Propagation, IEEE Transactions on*, 14(3):302–307, 1966.

Vita

Evangelos Anastasios Meintanis graduated from the 1st lyceum of Kifisia in 1993. He entered the Department of Physics at the University of Athens the same year and received his Ptychion in the summer of 1999. He entered the Graduate School at The University of Texas at Austin in September, 1999. He received a Master of Arts in physics in December, 2003.

Permanent Address: Pegasu 4
14564 Kifisia
Athens
Greece

This dissertation was typeset with LaTeX 2_ε[1] by the author.

---

[1] LaTeX 2_ε is an extension of LaTeX. LaTeX is a collection of macros for TeX. TeX is a trademark of the American Mathematical Society. The macros used in formatting this dissertation were written by Dinesh Das, Department of Computer Sciences, The University of Texas at Austin, and extended by Bert Kay, James A. Bednar, and Ayman El-Khashab.